2. STELLARATOR PHYSICS

James F. Lyon
James A. Rome
John L. Johnson
David T. Anderson
Paul R. Garabedian

Contents

2.1. INTRODUCTION 2-1
- 2.1.1. Stellarator Advantages and Drawbacks 2-1
- 2.1.2. Design of Stellarator Coil Configurations 2-2
- 2.1.3. Types of Stellarator Configurations 2-4
- 2.1.4. Separation of Physics and Cost Optimizations 2-5
- 2.1.5. Comparison of Different Stellarator Configurations 2-6
- 2.1.6. Selection of the MHH Configuration for the SPPS 2-11

2.2. THE MHH CONFIGURATION 2-13
- 2.2.1. Origin of the MHH Configuration 2-13
- 2.2.2. The MHH Magnetic Surface Geometry 2-13
- 2.2.3. Coil Engineering Issues 2-20

2.3. MHD EQUILIBRIUM AND STABILITY 2-23
- 2.3.1. Basis of β Limits in Stellarators 2-23
- 2.3.2. Sensitivity of the Equilibrium Configuration to β 2-24
- 2.3.3. Stability Considerations 2-29
- 2.3.4. Bootstrap Currents 2-29
- 2.3.5. Configuration Improvement 2-30

2.4. TRANSPORT 2-30
- 2.4.1. Global Scaling Laws for Stellarators 2-31
- 2.4.2. Comparison with Tokamak Scaling 2-32
- 2.4.3. Improvement in Confinement 2-32
- 2.4.4. Density Limit 2-34
- 2.4.5. Transport Modeling 2-34
- 2.4.6. Plasma Heating Options 2-40

2.5. PARTICLE AND HEAT REMOVAL 2-41
- 2.5.1. Separation of Particle and Heat Removal 2-41
- 2.5.2. Magnetic Geometry and Islands 2-42
- 2.5.3. Divertor Geometry 2-45

2.6. IMPROVEMENTS TO THE MHH PHYSICS BASIS 2-55
- 2.6.1. Validation of the MHH Physics Basis 2-55
- 2.6.2. Options for Configuration Improvement 2-56
- 2.6.3. The MHH3 Stellarator 2-58

REFERENCES 2-62

2. STELLARATOR PHYSICS

2.1. INTRODUCTION

Both tokamaks and stellarators are based on helical (toroidal plus poloidal) magnetic fields that produce toroidally nested, closed magnetic surfaces. This results in similar plasma confinement and stability properties for the two configurations. In tokamaks, the stabilizing toroidal field component is produced by a toroidal set of coils (TF coils) and most of the confining poloidal field is produced by a large toroidal current induced in the plasma. In stellarators [1, 2], both components of the magnetic field are created by currents flowing solely in external coils. Because the poloidal magnetic field that produces the rotational transform ι ($\iota = 1/q$, where q is the safety factor) of the magnetic field is created by currents outside the plasma, the plasma is inherently nonaxisymmetric; the plasma cross section changes shape as it rotates around the (sometimes noncircular and nonplanar) magnetic axis. The plasma aspect ratio $A_p \equiv R_0/a_p$ is generally larger than in a tokamak because the larger toroidal effects at smaller aspect ratio can produce field components that break the stellarator's helical symmetry. However, the field structure can be designed to reduce or even eliminate (a "quasi-helically symmetric" configuration [3]) this finite-aspect-ratio effect. Here R_0 is the average major radius of the torus and a_p is the average radius of the noncircular last closed flux surface (LCFS).

2.1.1. Stellarator Advantages and Drawbacks

Stellarators have some important potential operational advantages as fusion power plants. The absence of a net plasma current leads to inherently steady-state operation. There is no need for continuous power input to the plasma to maintain the magnetic configuration, so the reactor plasma can be truly ignited rather than having a high Q as in a tokamak. Here Q is the ratio of the fusion power produced to the plasma input power. Current drive power is not needed, which leads to higher plant efficiency, and there would be no current-drive-related reliability problems, which leads to higher plant availability. There are no dangerous current-driven disruptions or vertical stability problems, so a thick vacuum vessel is not required for equilibrium control or to protect against damage to it and the blanket structure. No pulsed magnetic or thermal loads occur, so there is no cyclic stress or $d\mathbf{B}_\perp/dt$ constraint on the superconducting coils. In

addition, there is a wide range of magnetic configurations possible with increased flexibility and control for optimization. The plasma parameters and profiles do not need to satisfy simultaneous (and often conflicting) constraints on disruption avoidance, density and beta limits, bootstrap current fraction, current drive efficiency, divertor performance, and improved confinement. Thus stellarators should be better able to operate in a true ignited steady-state fashion with time-invariant plasma profiles. The larger aspect ratio may also allow access from both the inboard (larger central hole) and outboard sides for easier maintenance.

Stellarators also have some potential drawbacks as fusion power plants. The larger aspect ratio leads to larger size. Although the resulting lower power density leads to longer component life, the larger size means more structure and consequently higher cost. The helical geometry requires more complex modules and more costly maintenance procedures. The smaller distance between the plasma and the coils leads to more restricted access and a more difficult divertor geometry, and hence more complicated maintenance and additional cost. It is the aim of this study to assess these advantages and drawbacks.

2.1.2. Design of Stellarator Coil Configurations

The most general form of the stellarator can have currents distributed throughout three-dimensional (3-D) space. A subset, still very general, of all possible stellarator configurations is a topologically toroidal system with currents distributed on a torus, subject only to the constraint that the current density $\mathbf{j}$ be divergenceless ($\nabla \cdot \mathbf{j} = 0$). Divergence-free currents on a torus can close either helically, poloidally, or toroidally. The first case creates helical coils (although in general they do not necessarily have large current-free gaps). The second case creates a nonplanar modular coil set. The toroidally-linked case has not been studied very much. In general, the same magnetic configuration can be created using any of these coil configurations. The appropriate choice is based upon engineering design of the resulting coil set; some magnetic configurations are more conveniently created using modular coils and some using helical windings.

Historically, there have been two design approaches used to create specific stellarator configurations: starting from a parameterized coil set or from desired physics properties.

Starting from coils. The more traditional design approach starts from the basic coil geometry, which can be described by a set of adjustable parameters. A set of "goodness" criteria is used as an optimization goal and the coil parameters are adjusted by a multidimensional optimization code. As each parameter is changed, the magnetic flux surfaces

are computed, the magnetohydrodynamic (MHD) equilibrium and stability properties are evaluated, and the other components of the goodness criteria are evaluated. In this approach, a small change in a coil parameter can lead to a large change in the resulting configuration so, in a sense, this approach is mathematically unstable because a small change can suddenly destroy the flux surfaces. The low-aspect-ratio torsatron CT6 was the result of applying this method using as a goodness criterion that it should have physics properties similar to those of the Advanced Toroidal Facility (ATF), but with a lower aspect ratio. The flexible heliac configuration TJ-II was optimized to have higher rotational transform, a global magnetic well, and a higher beta limit. It features a set of planar TF coils whose centers follow a helical path around central circular and helical coils that link the TF set.

Starting from physics properties. A systematic methodology [4, 5] for choosing a stellarator configuration with desired physics properties has been developed at the Max-Planck-Institut für Plasmaphysik (IPP) in Garching, Germany, building on theory and computer codes developed at New York University [6]. This approach is based upon the fact that the plasma boundary shape and pressure distribution are sufficient to determine the properties of the magnetic configuration. The boundary (LCFS) shape can be optimized to approximate an *a priori* defined set of magnetic properties (such as rotational transform, shear, magnetic well depth, and Fourier spectral content of the magnetic field). While neither the existence nor the uniqueness of a stellarator configuration with the desired properties is guaranteed (for a given set of conditions), this approach does provide a powerful methodology for searching for stellarator configurations.

Once a desired plasma boundary shape is derived from runs of the NSTAB [7] and TRAN [8] codes, the NESCOIL code [9] developed by P. Merkel, also at IPP Garching, can be used to find a set of coils of either helical or modular type to approximately produce the desired LCFS. A potential problem can be solved for the current lines on a chosen surface using the fact that the magnetic field $\mathbf{B}$ lies in a flux surface. The type of current line closure is solely dependent on the boundary conditions applied to this potential. This current distribution can be discretized to simulate 'coils' and the resulting error fields at the plasma boundary produced by real coils can then be calculated to check the degree of approximation to the desired configuration. The shape of the current surface can be optimized to meet a series of engineering side conditions such as constraints on the current density and the current-line curvature, as well as minimizing the error on the boundary, to arrive at a final model for a physical coil set.

The design of the newer modular stellarators, such as the Wendelstein 7-X (W7-X) or the Modular Helias-like Heliac (MHH), is based on analysis of the Fourier expansion of the magnetic field strength B in terms of Boozer's flux coordinates [10] in which the $\mathbf{B}$ lines are straight, the Jacobian is $1/B^2$, ψ is the toroidal flux, and ϑ and φ are poloidal and toroidal angle variables.

$$1/B^2 = \sum b_{m,n}(\psi)\cos(m\vartheta - n\varphi)\,, \tag{2.1-1}$$

Theory shows that the Fourier coefficients $b_{m,n}$ control most physical properties of the configuration. Good equilibrium, stability, and transport properties are achieved by reducing the size of the $b_{m,n}$'s for selected values of the indices m and n. This allows avoiding gross changes in the magnetic axis position or rotational transform profile as the plasma beta increases. The Fourier coefficients $b_{m,n}$ are in turn related to the Fourier coefficients $r_{m,n}$ and $z_{m,n}$ in the 3-D representation of the plasma surface,

$$r = \sum r_{m,n}\cos(m\theta + nM\phi)\,, \tag{2.1-2}$$

$$z = \sum z_{m,n}\sin(m\theta + nM\phi)\,, \tag{2.1-3}$$

where r, z, and ϕ are the usual cylindrical coordinates, M is the number of toroidal periods, and θ is a poloidal angle variable. See also Eq. (2.6-3) below, where the coefficients $\delta_{m,n}$ are defined that have a diagonally dominant relationship to the spectrum $b_{m,n}$, after a shift of 1 in the index m.

The NESCOIL method was used to determine the W7-X coil configuration using the "helias" optimization criteria in which finite-beta plasma currents are minimized (to preserve the vacuum-field properties at finite beta) and the orbit containment at high beta is improved due to the self-dug magnetic well. The MHH configuration chosen for this Stellarator Power Plant Study (SPPS) has features of both the helias and the heliac, and was also designed using this method [11].

2.1.3. Types of Stellarator Configurations

In general, there are four types of stellarators in operation: conventional stellarators, torsatrons (or heliotrons), heliacs, and modular stellarators. Conventional stellarators and torsatrons are based upon helical coils. In conventional stellarators, these coils are in pairs with opposite currents so that they produce no net toroidal field; additional TF coils are thus required. In torsatrons, the helical currents flow in the same direction so no TF coils are required. However, depending on the winding law, torsatrons may require

large vertical field coils. Generally, torsatrons are preferred over conventional stellarators due to their simpler coil configuration.

Torsatron reactors [12] typically have moderate plasma aspect ratio ($A_p \approx 3.3 - 8$), large magnetic shear (change in ι across the plasma), significant helical field ripple (up to $\sim 20\%$ at the plasma edge), and large access between the helical windings for blankets and maintenance. Modular stellarator reactors [13] typically have larger plasma aspect ratio ($A_p \geq 10$), small shear, smaller effective helical field ripple, blankets between the plasma and the coils, and divertors located inside the coils. Conventional heliacs have only received cursory examination [14] partly because of their linked coil geometry.

2.1.4. Separation of Physics and Cost Optimizations

The performance of a particular stellarator configuration as a reactor is determined by its physics properties (determined by a set of dimensionless parameters – its aspect ratio, rotational transform, shear, magnetic well depth, and other properties of the magnetic field) and the major device parameters: on-axis magnetic field strength, $\mathbf{B}_0$, and major radius, R_0. The fusion power core cost depends primarily on the mass (volume) of its major components (blanket, shield, and coils), and hence almost entirely on R_0.

The minimum size (R_0) for a stellarator core is determined by the minimum distance Δ between the edge of the plasma (LCFS) and the centerline of the nearest helical winding or modular coil because the ratio $A_\Delta \equiv R_0/\Delta$ is a constant for a given stellarator configuration. This is not a constraint for tokamaks because the position of the plasma edge and the edge configuration properties, other than the toroidal field ripple, do not depend on the proximity of the TF coils. The helical windings must be relatively close to the plasma edge in torsatrons to produce the edge shear needed for MHD stabilization, and the non-planar TF coils must be relatively close to the plasma edge in modular stellarators to permit practical coil designs. In both cases, an optimized magnetic configuration requires precise shaping of the external current paths; the resulting higher-order field components decay rapidly away from the windings, necessitating closeness to the plasma to avoid excessively large coil currents.

The minimum size for a stellarator core is thus given by $R_0 = A_\Delta d$, where d is the distance required for the plasma-wall separation, the first wall, the tritium breeding blanket, the neutron shielding, the coil dewar, the structural case facing the plasma, the half-radial depth of the coil winding pack, and assembly clearances. The cost of the most expensive reactor core components (blankets, shield, and coils) is related to the mass (volume) of

Table 2.1-I.
Characteristics of the Four Stellarator Configurations Studied and the Second-Stability ARIES-IV Tokamak

	CT6	MATF	MHH	Helias	ARIES-IV
No. of toroidal field periods, M	6	12	4	5	1
No. of main field coils	2	12	32	50	16
Center safety factor, $q_0 = 1/\iota(0)$	2.9	2.9	0.91	1.2	2.0
Edge safety factor, $q_a = 1/\iota(a)$	1.05	1.05	0.81	1.03	12.2
Average coil aspect ratio, R_0/a_c	2.5	4.6	3.3	5.0	1.0
Average plasma aspect ratio, R_0/a_p	3.8	10	9.7	13	2.8
Average plasma elongation, κ	2.1	1.7	2.0	2.0	2.0
Minimum plasma-coil separation ratio, R_0/Δ	6.4	7.2	7.0	12	3.2

these components and in turn to the plasma surface area [$\propto R_0 a_p \propto (A_\Delta d)^2/A_p$]. The smaller values of A_Δ obtained for a compact torsatron [15] allow this configuration to be a factor of 2–3 smaller in size than previous modular stellarators; typically $R_0 \approx 8 - 10$ m versus $R_0 \approx 20 - 25$ m. The reference MHH studied for the SPPS has $R_0 = 14$ m.

2.1.5. Comparison of Different Stellarator Configurations

Four stellarator coil configurations were examined in this study: (1) CT6, a Compact Torsatron with 2 large continuous helical windings, 6 field periods, and low plasma aspect ratio ($A_p = 3.8$); (2) MATF [16], a torsatron with modularized helical windings, 12 field periods, and $A_\mathrm{p} = 10$; (3) MHH [16], a modular helias-like heliac with 4 field periods and $A_p = 8.1$; and (4) the W7-X modular helias configuration [17] with 5 field periods and $A_p = 12.2$. The properties of these magnetic configurations are compared with those of the second-stability ARIES-IV tokamak reactor in Table 2.1-I.

The best-studied stellarator reactor configurations have been the modular helias stellarator [18] and the CT6 torsatron. The CT6 configuration (shown in Fig. 2.1-1) features two large continuous helical optimized for operation in the second stability region. The relatively large shift of the magnetic axis with increasing beta broadens and deepens the magnetic well to achieve higher beta. The helias configuration (shown in Fig. 2.1-2) features 50 nonplanar poloidal coils. It has been studied extensively at IPP Garching and forms the basis for the proposed W7-X experiment and the Helias Stellarator Reactor (HSR) studies [19]. It relies on the opposite physics optimization approach in which the magnetic geometry does not change much with increasing beta.

The two new coil configurations developed in this study were MHH and MATF. The MATF configuration (shown in Fig. 2.1-3) is based on a modularization of the ATF torsatron [20], similar to the earlier "symmotron" [21], but the modules are not up-down symmetric. The windbacks (40° above and below the equatorial plane) provide most of the required vertical field. The legs connecting the helical coil segments to the toroidal windbacks are perpendicular to the torus, which minimizes the field interaction with the torus and preserves most of the physics properties of the unmodularized coil configuration. The coil geometry allows field lines to exit between the windings to an exterior divertor chamber. The physics properties of MATF are similar to those of the ATF torsatron with continuous helical windings, except that MATF has better orbit confinement and smaller A_Δ.

The MHH coil set (shown in Fig. 2.1-4) is a modularization of a highly modulated heliac whose flux surfaces are helias-like, rather than bean-shaped as in the usual heliac. The reference MHH has four field periods with eight coils per field period. The MHH plasma geometry has some similarities to the W7-X helias configuration, but MHH has 4 field periods instead of 5, less triangularity of the flux surfaces, and a larger helical axis excursion. As in a helias, the plasma separatrix permits a helical divertor on the top and bottom. MHH's physics properties are similar to those of the helias configuration except that it has lower plasma aspect ratio, a larger bootstrap current, and more space between the last closed flux surface and the center of the coil winding surface. The value of A_Δ is smaller than in helias because much of the rotational transform is produced by the large helical excursion of the magnetic axis; there is also less indentation of the plasma surface, and the required physics properties have been relaxed somewhat. Nevertheless, numerical nonlinear stability tests with the NSTAB code [7] indicate that the plasma should be stable at $\langle\beta\rangle = 5\%$ and Monte Carlo orbit calculations indicate that its confinement properties should be similar to that for helias [22]. Here $\langle\beta\rangle$ is the volume-average value of the plasma beta.

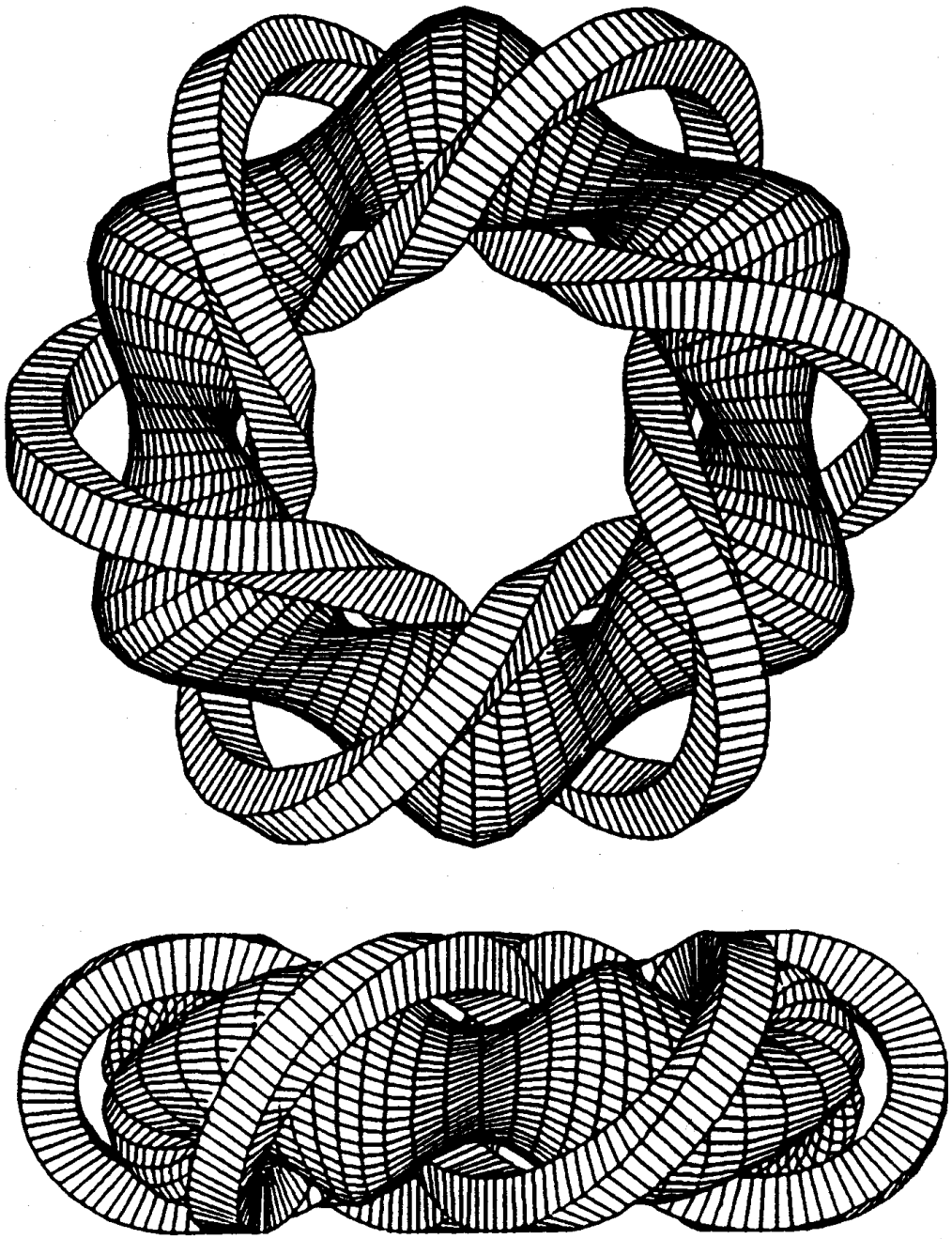

Figure 2.1-1. Top and side views of the CT6 helical coils and the last closed magnetic surface. A set of vertical field (VF) coils on the inboard side (not shown) is also needed for shaping control.

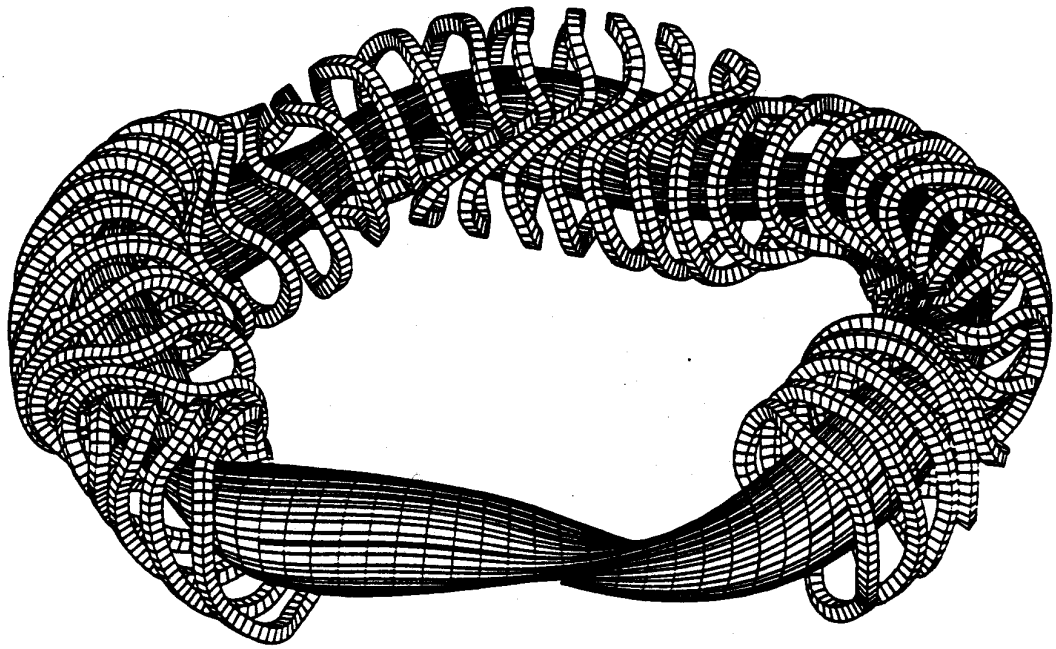

Figure 2.1-2. An oblique view of the helias configuration showing the nonplanar coils and the last closed flux surface.

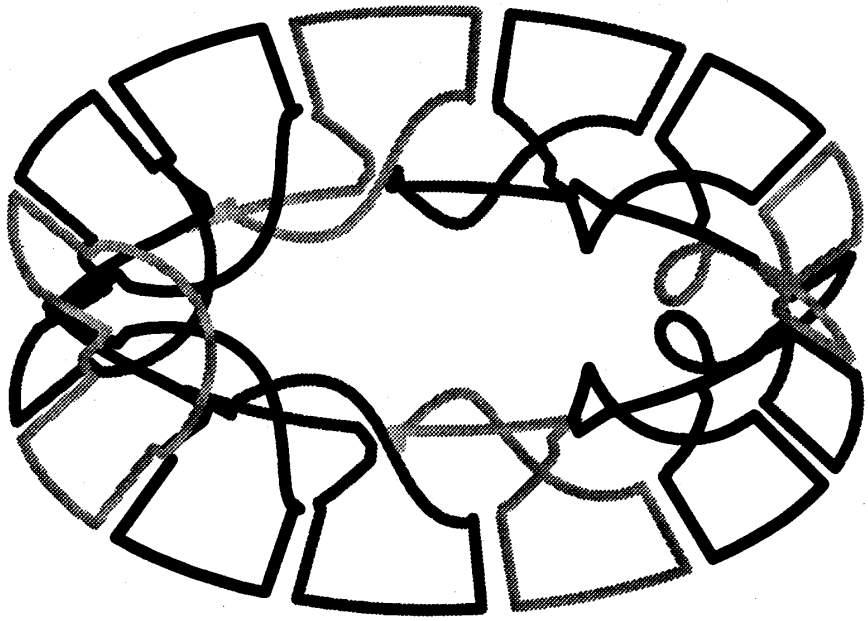

Figure 2.1-3. An oblique view of the 12 MATF coil modules.

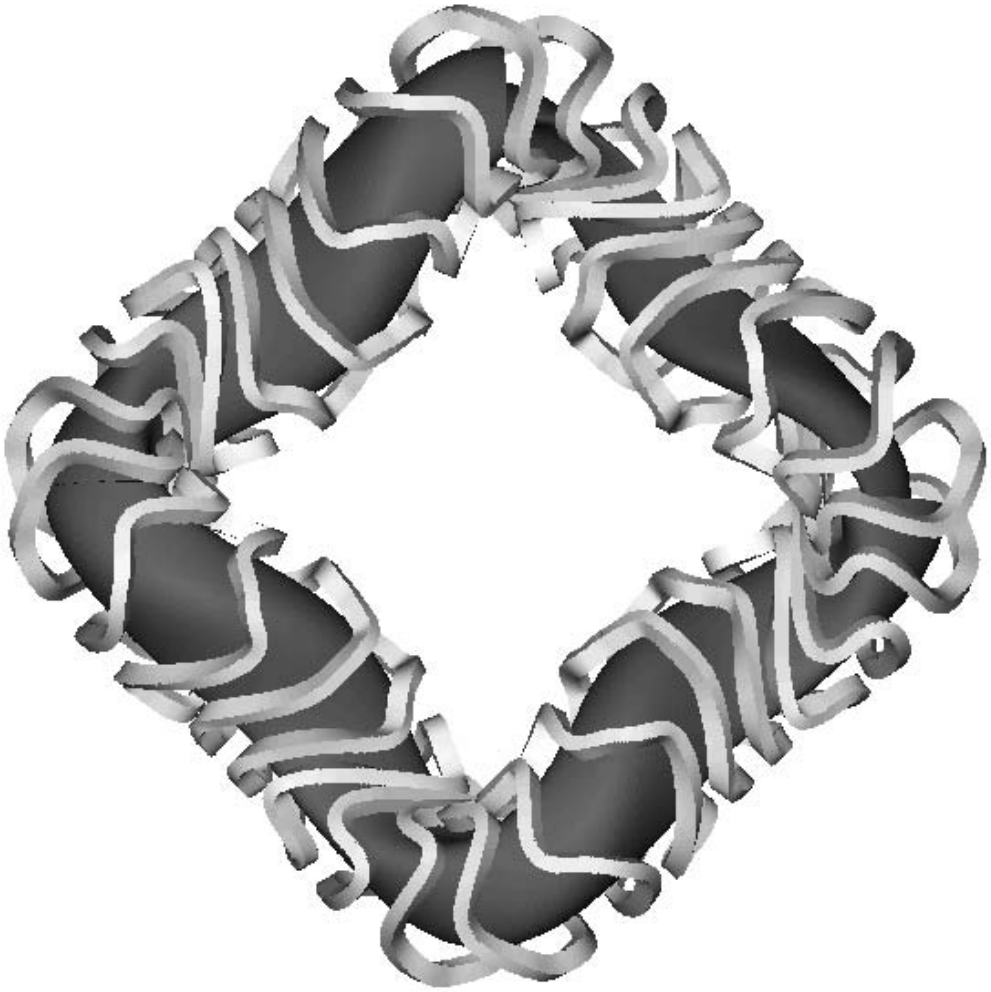

Figure 2.1-4. A top view of the MHH configuration showing the nonplanar coils, the blanket/shield structure, and the last closed flux surface.

2.1.6. Selection of the MHH Configuration for the SPPS

Four 1-GW(e) stellarator reactors were compared [16] by minimizing their cost for the same physics and engineering constraints. Table 2.1-II, reproduced from Ref. [16], compares the plasma and device parameters for these configurationsto the corresponding values for the second-stability tokamak reactor ARIES-IV [23]. The stellarator configurations are: (1) the 6-field-period Compact Torsatron CT6 with two large continuous helical windings, $R_0 = 12$ m and $B_0 = 4.6$ T; (2) the 12-field-period torsatron MATF with 24 modular coils, $R_0 = 13$ m and $B_0 = 5.5$ T; (3) the 5-field-period helias with 50 modular coils, $R_0 = 23$ m and $B_0 = 4.1$ T; and (4) the 4-field-period helias-like heliac MHH with 32 modular coils, $R_0 = 13$ m and $B_0 = 5.3$ T. The minimum size (hence cost) of these configurations was determined by their A_Δ value and the space d between the plasma and the coils needed for blanket, shield, structure, spacing, *etc.* Smaller R_0 can be obtained for less-conservative blanket and shield assumptions. Table 2.1-II shows that both MATF and MHH are competitive with ARIES-IV. The magnetic fields on axis and at the coils for both are less than those for ARIES-IV, although the coil geometry is more complex.

The MHH configuration was chosen for the SPPS because its helias-like features led to good physics properties and its heliac feature, the large helical excursion of the magnetic axis that provides most of the rotational transform, allows the coils to be farther from the plasma, permitting a 2-m distance between the plasma and the coils for blankets, shields, structure, clearance, *etc.* for a 14-m average major radius. Here 14 m has been chosen instead of the 13 m in Table 2.1-II to allow for additional distance between the plasma and the centerlines of the coils. This new configuration has the best physics properties (beta limit, neoclassical transport, orbit losses, reduction of bootstrap current, *etc.*). However, its smaller plasma-coil separation leads to a larger major radius (larger blanket and shield area) and consequently higher cost. The CT6 configuration has good access between the coils for blankets and divertor and the large plasma-coil distance leads to moderate-size reactors. The large helical field ripple leads to increased orbit losses, which it turns out are not a problem [12]. However, the large continuous helical coils would be difficult to fabricate and repair. The MATF configuration remedied most of the CT6 drawbacks and was selected as a backup configuration.

Table 2.1-II.
Plasma and Device Parameters for Different 1-GW(e) Power Plants [16]

	CT6	MATF	MHH	Helias	ARIES-IV
Major radius, R_0 (m)	11.8	13.4	13.1	23.3	6.04
Average plasma radius, a_p (m)	3.1	1.3	1.4	1.9	2.2
Toroidal field on axis, B_0 (T)	4.6	5.5	5.3	4.1	7.6
Maximum field on coils, B_{max} (T)	14.0	13.7	15.4	8.7	15.9
Average plasma density, $\langle n \rangle$ (10^{20} m^{-3})	1.0	2.5	2.7	1.4	2.9
Average plasma temperature, $\langle T \rangle$ (keV)	8.1	6.8	7.0	8.1	10
Central ion temperature (keV)	26	22	24	26	27
Central electron temperature (keV)	29	25	24	26	27
Volume-average toroidal beta, $\langle \beta \rangle$	2.9%	4.3%	5.0%	5.0%	3.4%
Energy confinement time, τ_E (s)	4.1	1.6	1.4	2.4	1.5
Lackner-Gottardi confinement multiplier	2.0	2.0	1.5	1.7	2.5
Neutron wall loading, Γ_n (MW/m^2)	0.9	1.8	1.3	0.5	2.7
Fusion core mass (10^3 tonnes)	10.7	8.7	7.8	18.8	9.0
Cost of electricity (mill/kWeh)$^{(a)}$	70	62	66	100	68

(a) In constant 1992 dollars.

2.2. THE MHH CONFIGURATION

2.2.1. Origin of the MHH Configuration

In a conventional stellarator, the rotational transform is provided by the fringing field of the coils, which decays rapidly inward from the coils toward the plasma. If the rotational transform could be achieved by introducing a large helical excursion of the magnetic axis, then the remaining freedom in specifying the coil set could be devoted to improving the physics properties of the configuration and to increasing the plasma-coil separation. To achieve this goal, a configuration was devised using a set of axisymmetric circular coils (with different currents) arranged on a circular torus. Inside these coils, and linking them, there was a large $\ell = 1$ helical coil spatially modulated to produce flux surfaces with a cross-section that varied from triangular to bean-shaped. Outside the circular coils there was a second (smaller) helix that was used to control the shear and the magnetic well. This configuration, a "helias-like heliotron", is described in more detail in Ref. [11].

A modular coil set that creates the same magnetic configuration, but involves no interlocked coils, was developed using the Garching NESCOIL code [9]. This configuration [16], a Modular Helias-like Heliac (MHH), became the basis for the SPPS power-plant concept. Figure 2.2-1 shows the particular MHH coil set that was chosen. The configuration has four field periods with eight coils per period, for a total of 32 coils. Because of the stellarator symmetry, there are only four different types of coils in the coil set. If the configuration is viewed from the top, it resembles a square; magnetically, it resembles four linked mirrors. However, if viewed from the side, the large vertical excursion of the coils is evident. The MHH modular coils are highly modulated and are close together on the inside of the corners where the magnetic field strength is high. This corner region is the focus of many of the engineering difficulties faced by the coil designers.

2.2.2. The MHH Magnetic Surface Geometry

Figure 2.2-2 shows the outer (last closed) flux surface for the reference MHH case. The four-field-period nature and the pronounced helical distortion of the flux surface is evident in the figure. This surface is described by the set of Fourier coefficients $r_{m,n}$ and $z_{m,n}$ in Table 2.2-I. A partial symmetry in these coefficients can be seen; for most, but not all, of the m, n values, $z_{m,n} = -r_{m,n}$.

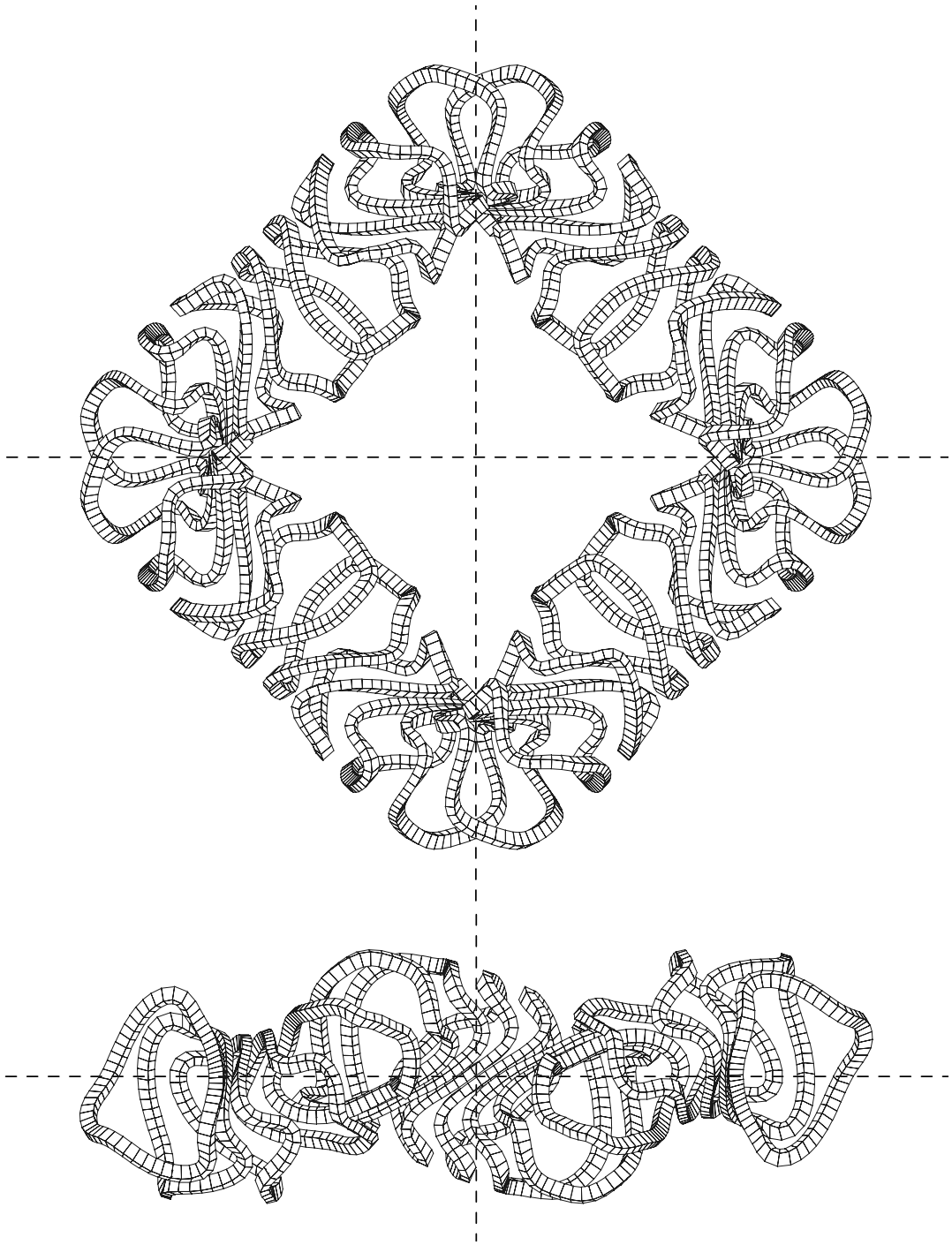

Figure 2.2-1. A top view and side view of the MHH coil set. The width represents the size of the conductor without the coil case. The side view is from the inside of the torus and shows the closeness of the corner coils at the center of the plot.

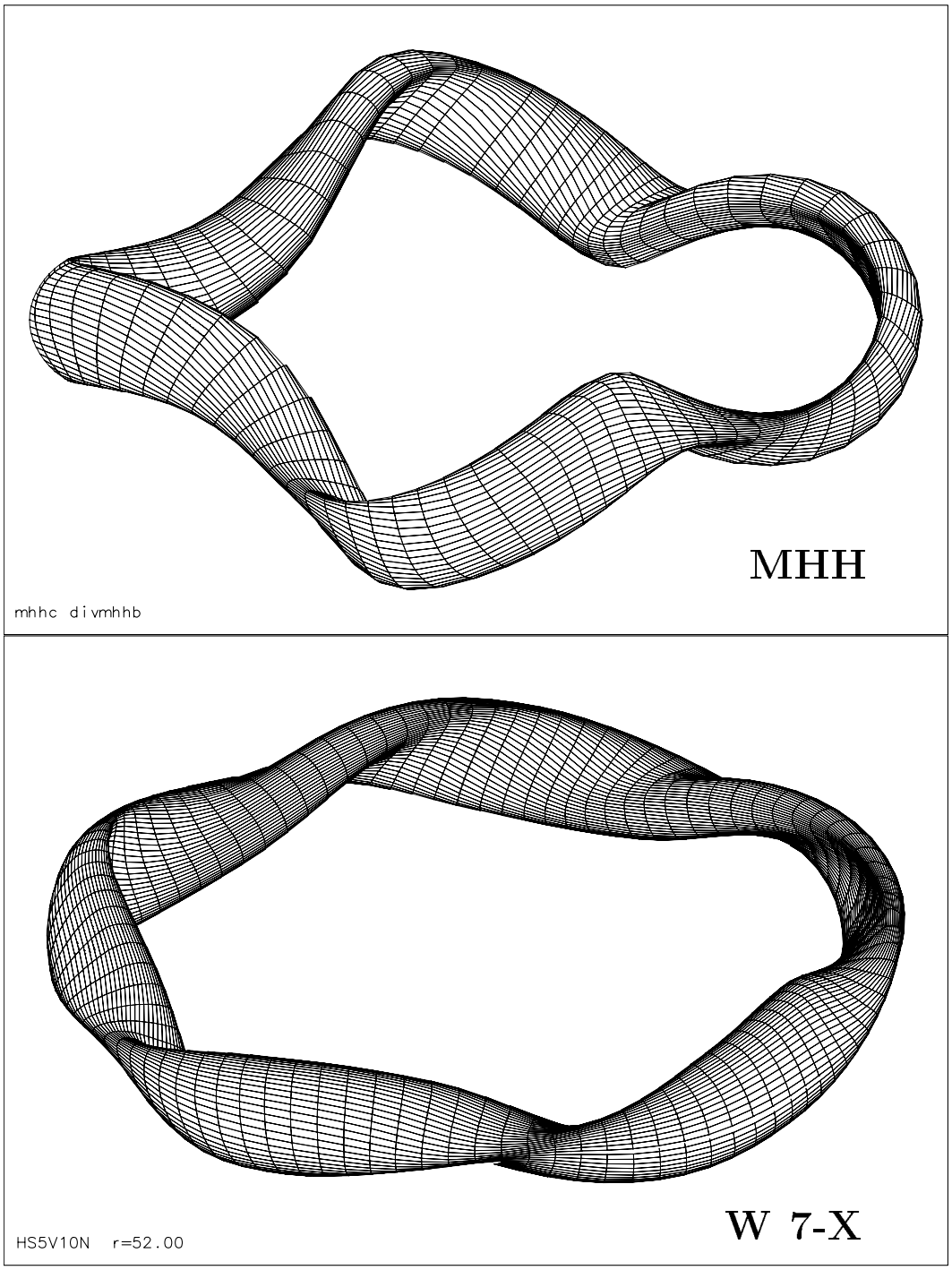

Figure 2.2-2. Comparison of the last closed flux surface for the reference MHH (top) and the W7-X helias (bottom).

Table 2.2-I.
Fourier Coefficients for the MHH Plasma Surface

	$r_{m,n}$			$z_{m,n}$		
n	$m=0$	$m=1$	$m=2$	$m=0$	$m=1$	$m=2$
–3	0.008			–0.008		
–2	0.1			–0.1		
–1	1.0	–0.1	0.05	–1.0	0.1	–0.05
0	6.2	–0.335	0.09		0.335	–0.09
1	0.13	0.8	0.07	–0.13	0.8	0.15
2		0.02	0.07		0.02	0.07
3		–0.02			–0.02	

Figure 2.2-3 shows three cuts through the magnetic surfaces; at the beginning, at 0°, 22.5°, and 45° field period. The inner solid curve is the "design" last closed flux surface (LCFS), and the outer solid curve is the coil winding surface (CWS). The design LCFS agrees quite well with the actual LCFS except for some distortion due to magnetic islands. The helical axisof MHH is also evident. The LCFS has some similarity to the helias configuration, as shown in Fig. 2.2-2, which compares the LCFS for MHH with that for W7-X. Figure 2.2-4 shows that the MHH configuration has a larger helical axis excursion and less triangularity than the W7-X configuration [24].

Figure 2.2-5 displays a contour plot of the distance between the LCFS and the CWS. Because of the contorted topology of the MHH configuration, the closest distance is not necessarily perpendicular to the LCFS. The minimum distance occurs on the inside of the triangular cross-section, and the minimum gap is 2 m for $R_0 = 14$ m. The gap is much larger at some other places (near the top and bottom in the lower part of Fig. 2.2-5).

Because MHH looks like a square when viewed from above, the term "major radius" is in some sense an "average" value. We define it to be the value of the $r_{0,0}$ coefficient in the Fourier series that describes the LCFS. It is more accurate to describe MHH in terms of its volumes and cross-sectional and surface areas, since these are the quanti-

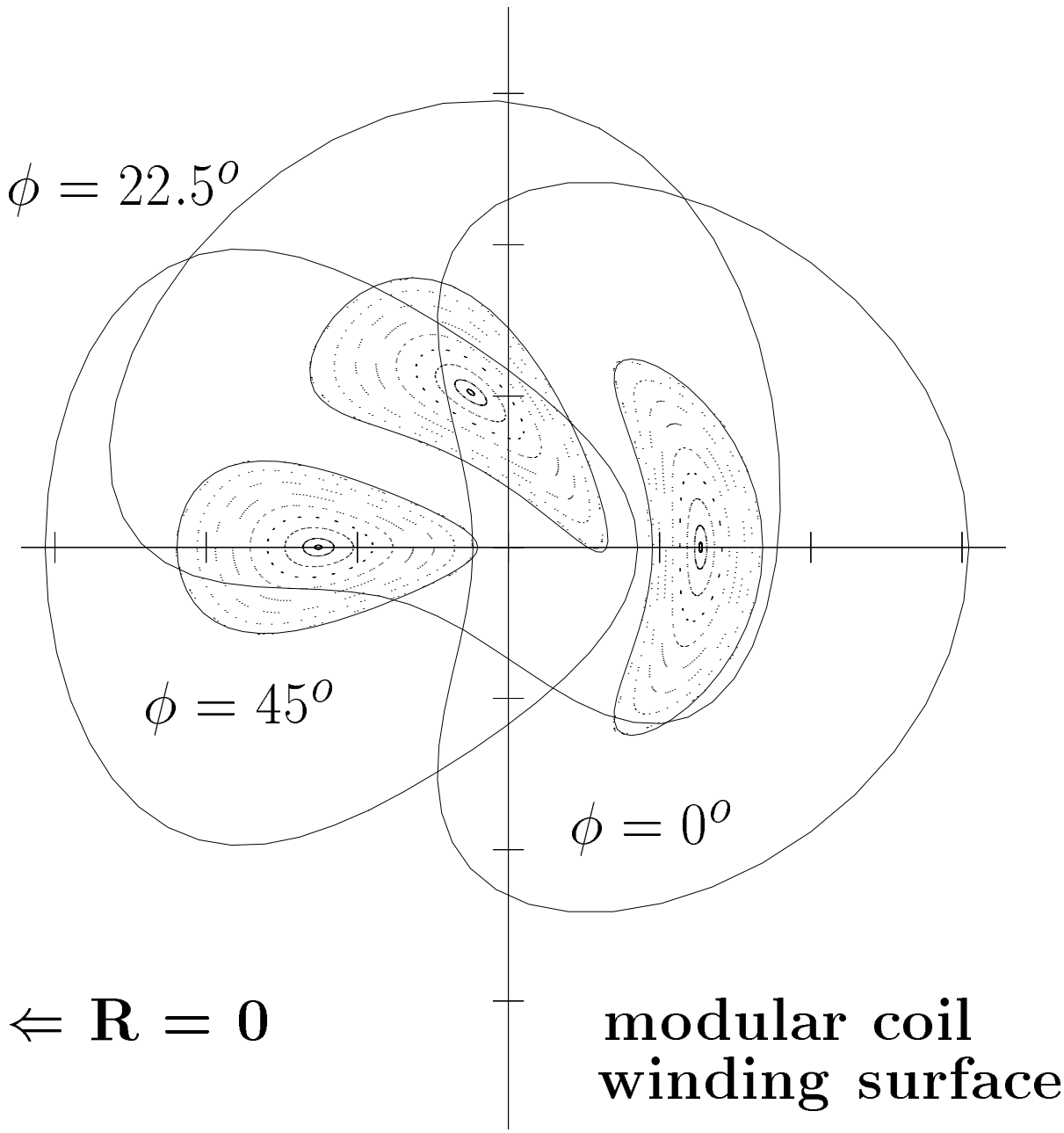

Figure 2.2-3. Magnetic surfaces at three toroidal angles for the MHH configuration showing the change from bean-shaped (at $\phi = 0°$) to teardrop-shaped (at $\phi = 22.5°$) to triangular (at $\phi = 45°$) — the helias-like feature — and the rotation of the magnetic axis about the average major radius R_0 — the heliac feature. The outer curves show the CWS cross section at these toroidal angles.

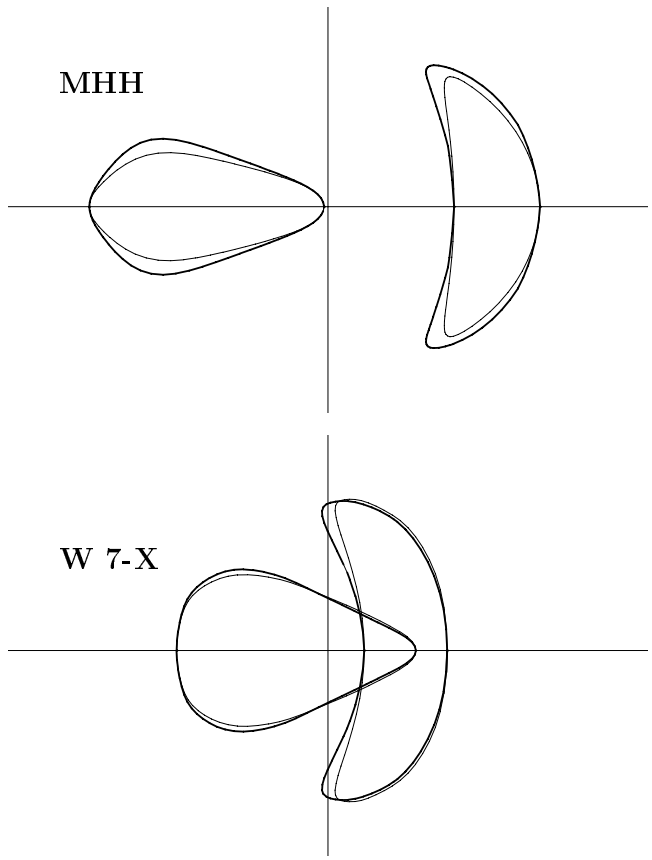

Figure 2.2-4. Comparison of the edge magnetic surface for MHH (top) and the W7-X helias (bottom) at $\phi = 0°$ (right) and at $\phi = 45°$ (left). The heavier (outer) curves are cuts at constant toroidal angles and the thinner (inner) curves are cuts perpendicular to the magnetic field **B**.

ties that can be properly calculated, and generally, they are the quantities required for physics and engineering calculations. The values for MHH, calculated using curvilinear formulas developed by S. Hirshman, are given in Table 2.2-II. Since the size of the MHH configuration can be scaled as appropriate, the actual size of the reactor embodiment is determined by external factors, usually the plasma-coil spacing. In order to make the minimum plasma-coil distance 2 m (as dictated by coil current density requirements and blanket and shield thickness), the major radius was scaled to 14 meters.

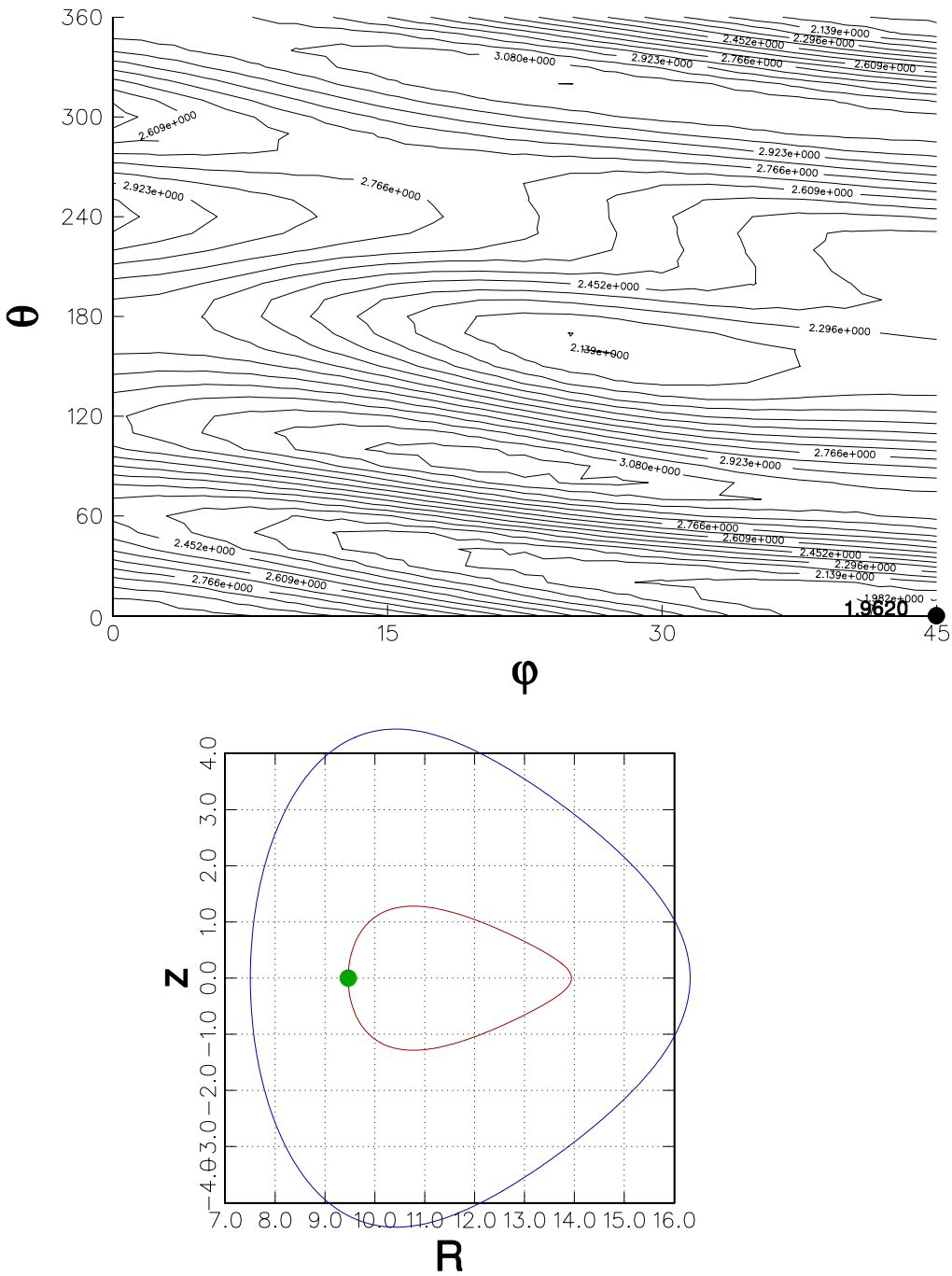

Figure 2.2-5. A contour plot of the distance between the LCFS and the CWS in the $\theta - \phi$ (poloidal angle-toroidal angle) plane. The lower part of the picture shows the point (•) where the spacing is smallest (at the inboard side of the torus).

Table 2.2-II.
Geometrical Characteristics of the MHH Configuration

	$R_0 = 10$ m $^{(a)}$	$R_0 = 14$ m
Plasma volume inside LCFS (m^3)	267.5	734
Plasma surface (LCFS) area (m^2)	629	1,233
Average plasma cross section (LCFS) (m^2)	4.29	8.4
Volume within coil winding surface (CWS) (m^3)	2,085	5,720
Area of coil winding surface (m^2)	1,495	2,930
Average cross-sectional area of CWS (m^2)	32.9	64.4

(a) Value normalized to $R_0 = 10$ m.

2.2.3. Coil Engineering Issues

Another set of issues centers on the engineering feasibility of the MHH coil set. Figure 2.2-6 shows the distance between the centerline of each coil and the neighboring coil as a function of position along the coil [24]. The spacing is tightest at the corners on the inside but is an order of magnitude larger at the outside in the straight sections. The final coil design allows room for the coil conductors, but requires that some of the intercoil case be eliminated in the inside corner regions. The maximum field in this area is also high. Figure 2.2-7 shows the $|B|$ contours for the coils and a 3-D plot of the same calculation [24]. The maximum field in the coil is about 14.5 T for a central field of 5 T; dealing with this is a major driver in the coil design. The fact that the high-field region in Fig. 2.2-7 occurs in a small region of the coil permits the use of graded conductors.

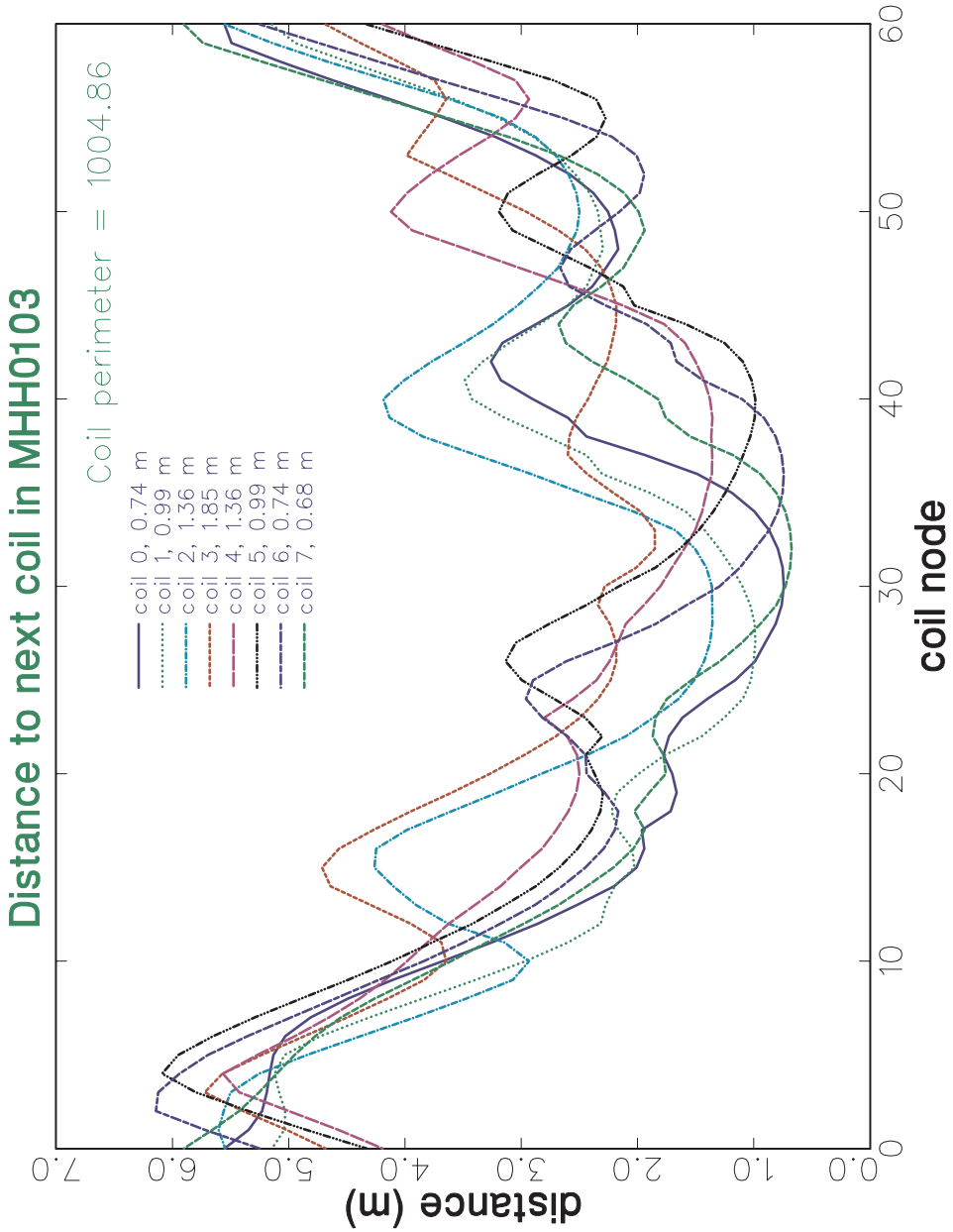

Figure 2.2-6. Distance from the centerline of each modular coil to the adjacent coil as a function of the poloidal distance along the coil. The curve labels indicate the coil number and the minimum distance to the nearest coil for $R_0 = 14$ m. The coil perimeter is 10.05 m.

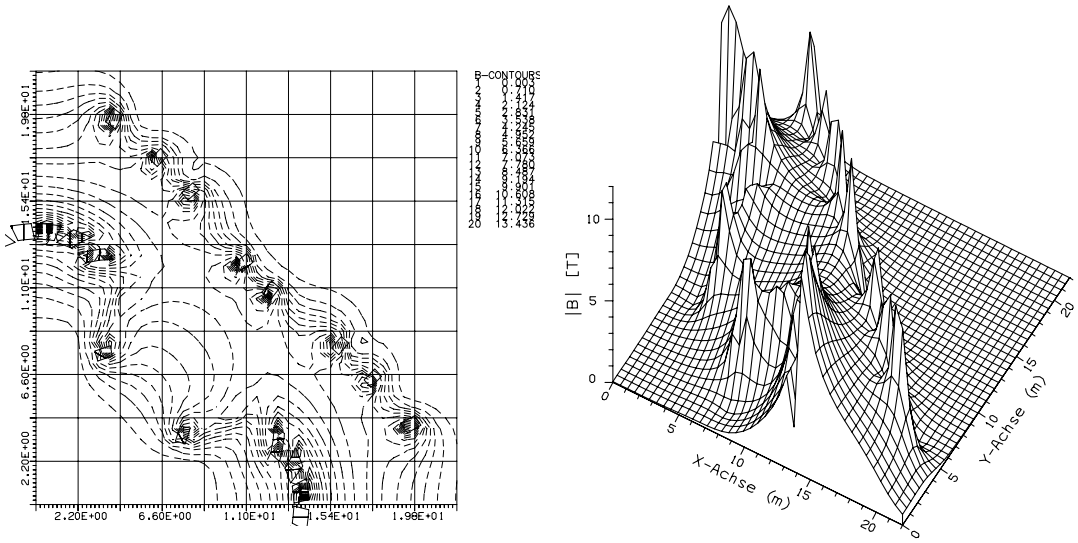

Coil system MHH-A: Magnetic field distribution of the first quadrant in the plane $z = 0$. Left: contour plot of the magnitudes, right: the same as a 3D-plot.

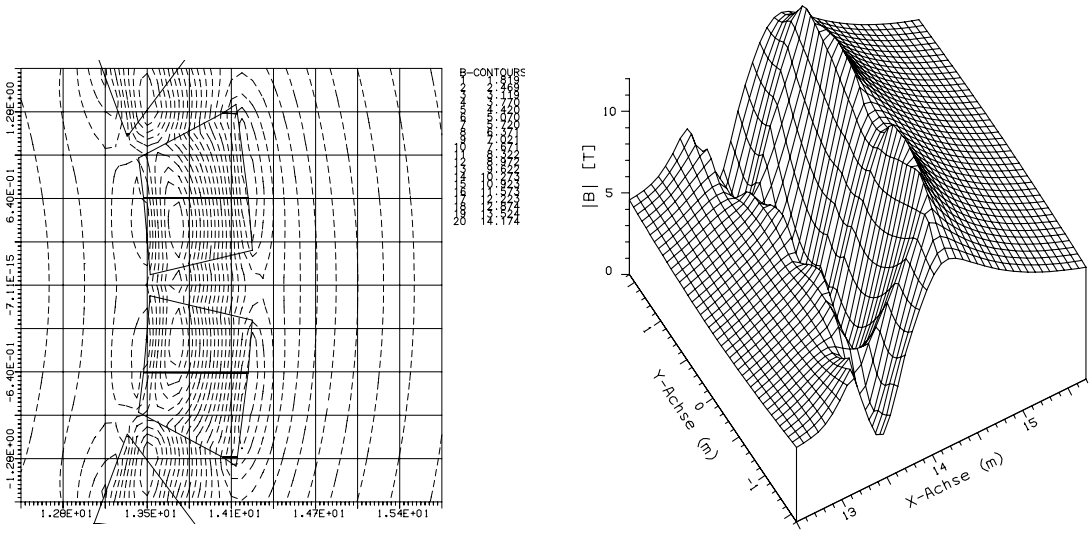

Coil system MHH-A: Magnetic field distribution near the coils 1 and 32 in the plane $z = 0$. Left: contour plot of the magnitudes, right: the same as a 3D-plot.

Figure 2.2-7. $|B|$ contours and an elevation plot of $|B|$ at the outside and inside of the coil set near the midplane.

2.3. MHD EQUILIBRIUM AND STABILITY

The MHH configuration was designed with the physics optimization techniques that have been developed at NYU [6] and at the Max-Planck-Institute für Plasmaphysik [4,5]. The studies that were used to design the coil system employed calculations of the magnetic field using the NSTAB equilibrium and nonlinear stability code [7]. In particular, the shape of the vacuum-plasma interface with $\langle\beta\rangle = 0$ was adjusted to optimize the physics and the necessary coil locations and currents were determined by means of the NESCOIL code [9]. This calculation was iterated to obtain satisfactory separation between the coils and forces on the coils. The major difference in the approach used in the design of W7-X and MHH is that the Garching optimization maximizes the physics properties whereas the SPPS imposes less stringent physics constraints to increase the space between the coils and the plasma for blankets and shields. This has led to a configuration in which physics issues must be considered. The most basic consideration is associated with large-scale plasma behavior, and is usually treated with simple MHD models. The relevent questions that arise concern the change in the equilibrium, the MHD stability behavior, and the bootstrap current as $\langle\beta\rangle$ is increased.

2.3.1. Basis of β Limits in Stellarators

As in a tokamak, the limits on $\langle\beta\rangle$ that must be observed in a stellarator come from both the equilibrium and the stability properties of the configuration. Probably the actual limiting value of β will occur when plasma currents distort the shape of the equilibrium configuration significantly, primarily by introducing magnetic islands that become sufficiently large or close to each other that they destroy the confinement. Pressure gradients in regions where the magnetic field lines have geodesic curvature cause Pfirsch-Schlüter currents (which are associated with the condition that the current be divergence-free and have a strong dependence on the poloidal angle) and bootstrap current (associated with poloidal viscosity causing the drifting ions to go preferentially in one direction). These currents in turn modify the shape of the configuration. The modifications of the configuration can be attributed primarily to the change in the rotational transform profile which can introduce and relocate resonant surfaces where mode coupling can strongly distort the magnetic field lines. Even if these modifications of the equilibrium configuration are not critical, the plasma currents can introduce MHD instabilities. Unlike the situation in a tokamak, where catastrophic disruptions driven primarily by the energy associated with the current in the toroidal direction must be controlled, the most damaging modes

in a stellarator are pressure-driven, ballooning or interchange instabilities that create a soft β-limit by enhancing the transport.

The helias configuration design that is being pursued in Garching addresses these problems by choosing an optimization that minimizes both Pfirsch-Schlüter and bootstrap currents and uses the self-dug well at finite β to improve confinement. This physics optimization results in a relatively small distance between the plasma and coils for the blanket and shield, which makes it essential to go to a larger size than is desired by American utility companies. The optimization that is used for the MHH design emphasizes engineering considerations and reduces, but does not eliminate the problems associated with pressure-driven plasma currents. The resulting configuration represents a reasonable compromise between the desire to simplify the engineering at the cost of not completely optimizing the physics. Indeed, the configuration that has been adopted for this study appears to be only marginally satisfactory from an MHD point of view. Some work on a related three-field-period configuration (Sec. 3.6.3) has shown that these problems may be ameliorated without seriously compromising the engineering considerations.

2.3.2. Sensitivity of the Equilibrium Configuration to β

The MHH vacuum-field equilibrium configuration, as calculated with the VMEC code [25], is shown in Fig. 2.3-1. The configuration with $\langle\beta\rangle = 4.8\%$, as calculated with the VMEC code with the plasma-vacuum interface kept fixed, is given in Fig. 2.3-2. The shape of the configuration is not drastically changed, but the plasma currents have shifted the magnetic axis outwards at the $\phi = 0°$ location. The Pfirsch-Schlüter current has, however, modified the shape of the rotational transform significantly, as can be seen in Fig. 2.3-3. The fact that an $m = 1$, $n = 1$ resonant surface has been introduced into the plasma region is of particular concern. Similar results to those presented in these figures were obtained with the NSTAB code [7].

Both of these three-dimensional (3-D) equilibrium codes utilize a weak formulation of the partial differential equations involved that circumvents questions of the nonexistence of solutions by introducing current sheets at resonant surfaces to prevent the appearance of magnetic islands. That the magnetic islands could produce a problem can be seen from a calculation of the equilibrium with $\langle\beta\rangle = 2.4\%$ that was done with the PIES code [26] which calculates the equilibrium configuration by integrating along the magnetic field lines and adjusting the pressure distribution on resonant surfaces where difficulties would otherwise occur. The results for this calculation are shown in Fig. 2.3-3 and in Fig. 2.3-4. It should be noted that islands have been introduced at several rational surfaces and one

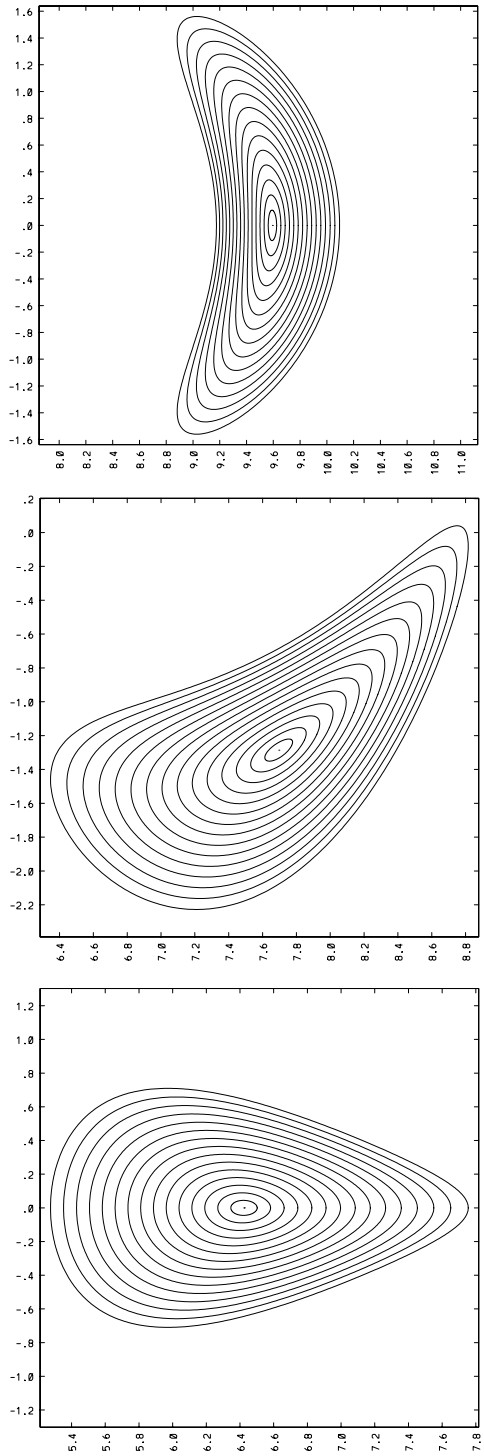

Figure 2.3-1. Vacuum field magnetic surfaces for the MHH configuration as computed with the VMEC code at $\phi = 0°$ (top), $\phi = 22.5°$ (middle), and $\phi = 45°$ (bottom).

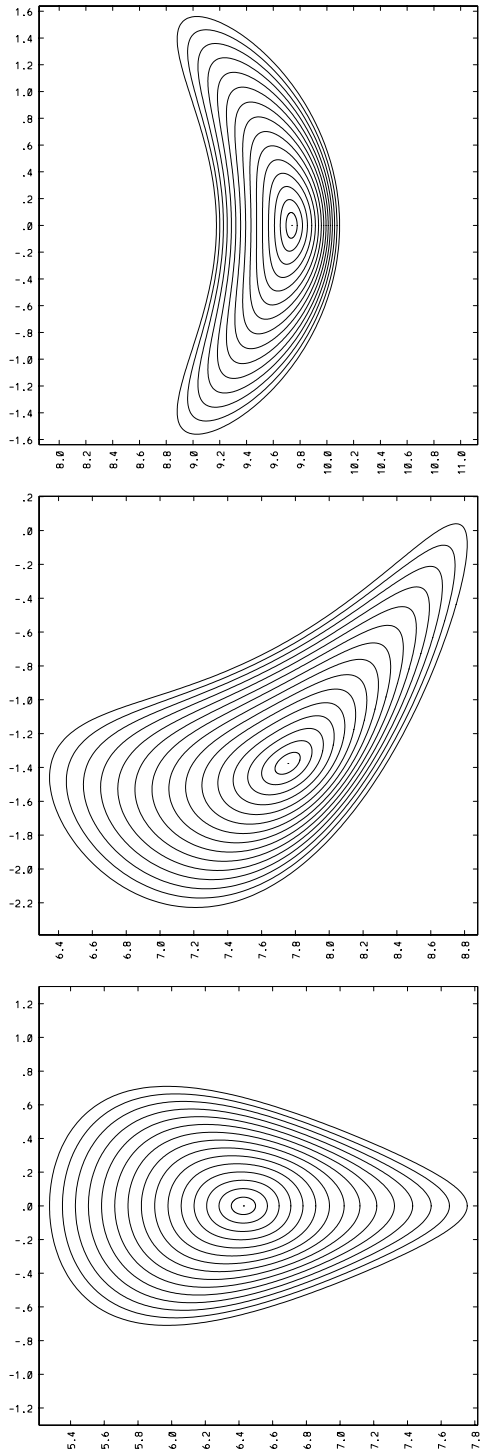

Figure 2.3-2. Magnetic surfaces for MHH configuration with $\langle\beta\rangle = 4.8\%$ as computed with the VMEC code at $\phi = 0°$ (top), $\phi = 22.5°$ (middle), and $\phi = 45°$ (bottom).

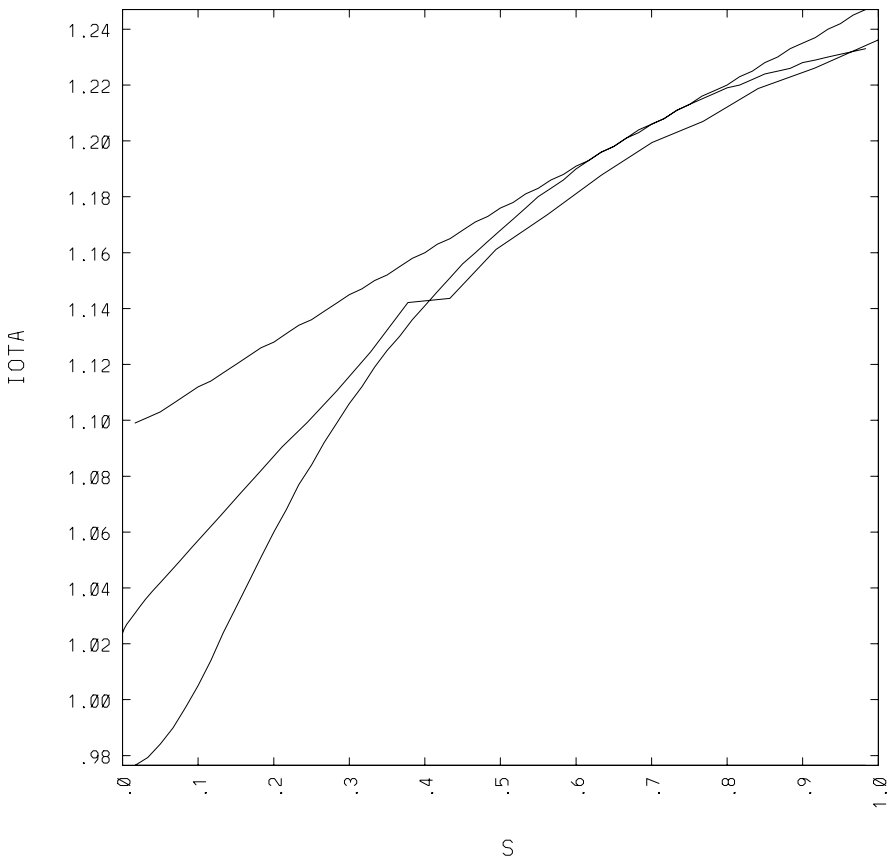

Figure 2.3-3. Rotational transform for the MHH configuration. The upper curve is for $\langle\beta\rangle = 0$ as calculated with the VMEC code; the middle curve is for $\langle\beta\rangle = 2.4\%$ as calculated with the PIES code, and the lower curve is for $\langle\beta\rangle = 4.8\%$ as calculated with the VMEC code.

has become sufficiently severe that it has led to a flattening of the rotational transform. Calculations with higher values of $\langle\beta\rangle$ with the PIES code have not been successful because of the presence of the $m = 1$, $n = 1$ resonant surface in the plasma. We believe that our difficulty has been due to numerical problems and that the actual configuration would be similar to that of Fig. 2.3-4 but with a larger island surrounding the $\iota = 1$ surface.

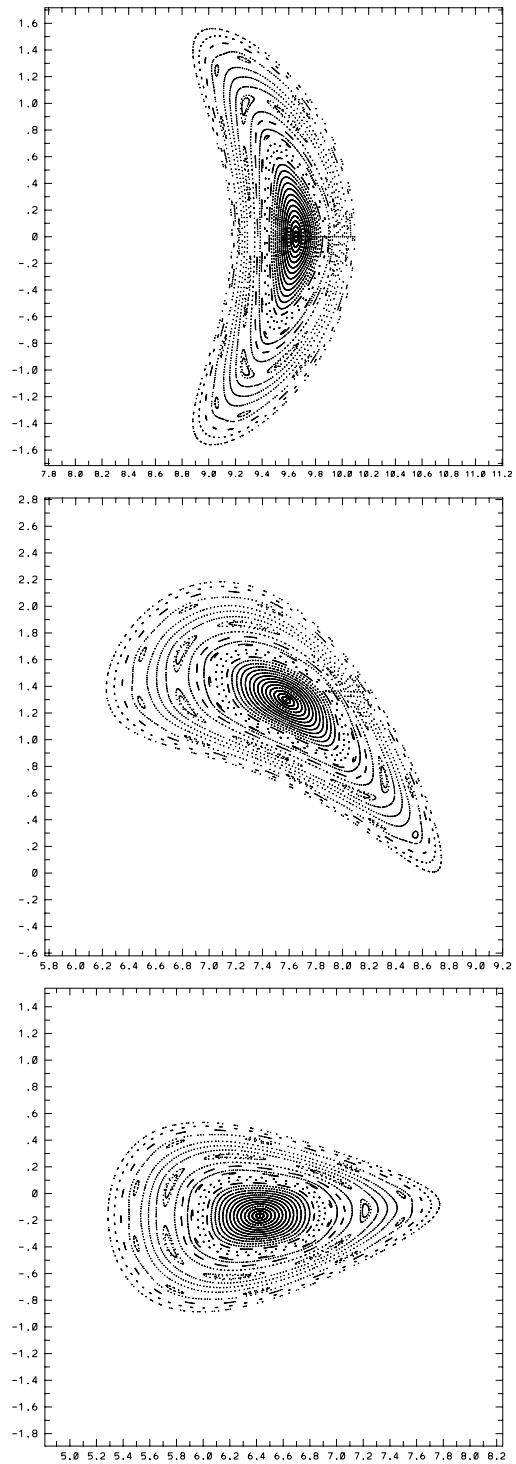

Figure 2.3-4. Magnetic surfaces for the MHH configuration with $\langle\beta\rangle = 2.4\%$ as computed with the PIES code at $\phi = 0°$ (top), $\phi = 22.5°$ (middle), and $\phi = 45°$ (bottom).

2.3.3. Stability Considerations

A major advantage that the stellarator possesses over the tokamak is that it does not have a large toroidal current that can provide energy to drive large-scale MHD instabilities like disruptions. Indeed, in a typical stellarator, and in the MHH configuration, the sign of the shear in the rotational transform is favorable even for ballooning modes, a "reversed-shear configuration" that has recently been favorably regarded by tokamak designers because of its superior stability properties. In the analysis of the MHH configuration, one can note that the driving forces for large-scale modes are small and the favorable shear makes ballooning studies less important, and thus calculate only the local stability functions D_I and D_R for ideal (Mercier) and resistive modes [27]. This has been done using the VMEC code studies of the case with $\langle\beta\rangle = 4.8\%$ where the configuration is marginally stable. It should be expected, but has not been shown, that localized ballooning modes will become unstable at or possibly below this value of $\langle\beta\rangle$ because of the lessening of the local field line shear due to the competition between the global twisting associated with the vacuum magnetic field and the local twisting introduced by the Pfirsh-Schlüter currents. These may not be severe since they would be centered at rational surfaces where the presence of magnetic islands would already have degraded the confinement. However, if such modes were serious, they should have been observed in some of the calculations using the NSTAB code; they did not appear and there was no indication of a flattening of the local pressure distribution.

2.3.4. Bootstrap Currents

A major concern in both tokamak and stellarator physics concerns the bootstrap current – in the tokamak it is essential to maximize it with care taken to obtain the proper spatial distribution so as to minimize the need for external current drive; in the stellarator it is desirable to minimize this current.

When the mean-free path in the plasma is long compared to its size, then the parallel viscosity component in Ohm's Law creates a bootstrap current. It arises when particles moving parallel to the magnetic field lines are displaced from their home flux surface by a different amount than those moving anti-parallel due to the particle drift motion. It is possible in a stellarator to reduce the net bootstrap current to zero (or even to reverse its direction [28]) because the bootstrap current component due to the helical component of the magnetic field is opposite to that associated with the toroidal component.

Boozer and Gardner [29] have shown that this current depends on the magnetic configuration only through the variation of the field strength on each magnetic surface $B(\psi, \vartheta, \varphi)$ and the rotational transform $\iota(\psi)$, and have provided a simple approximate expression that should apply if the fraction of trapped particles is small. Here ψ is the toroidal flux and ϑ and φ are poloidal and toroidal angle variables. Estimates of the bootstrap current in the MHH configuration with $\langle\beta\rangle = 4.8\%$ indicate that this current could cause a significant change in the rotational transform and thus seriously affect both the equilibrium and the stability properties of the device. Because the magnetic configuration is fairly complicated so that the simple model of few trapped particles may not be applicable, the SPPS has not examined the problem in sufficient detail. On the other hand, as discussed in the next section, it is reasonable to believe that a relatively straightforward modification of the configuration would solve this problem without introducing serious new engineering difficulties.

2.3.5. Configuration Improvement

Considerations of the reference MHH stellarator configuration indicate that there are, or could be, problems with all three aspects of MHD: equilibrium, stability, and bootstrap current. These problems can all be traced to the choice of the central-vacuum-field rotational transform being just above the value $\iota = 1$. A configuration (described in Sec. 3.6.3) in which the number of helical field periods is changed from $M = 4$ to $M = 3$, which would lower $\iota(0)$ to about 0.8 and $\iota(a)$ to about 0.95, can eliminate all of these problems. This change actually improves the engineering problems concerning supporting the magnetic field coil forces and providing room for the blankets and shields. Since this modified configuration had not been determined before a significant part of the engineering studies were underway, the original configuration was used for the study.

2.4. TRANSPORT

MHD considerations set a constraint on the plasma performance through either greatly enhanced transport (a "soft" beta limit) due to the onset of larger magnetic islands or a more severe limit due to overlapping islands. Below this limit, the more usual transport considerations determine the plasma performance. Although there are some theoretical models for transport, especially at low collisionality [30], performance predictions, as in tokamaks, are better based on empirical confinement scaling "laws".

However, Monte-Carlo calculations using the TRAN code played a significant role in arriving at the MHH configuration.

2.4.1. Global Scaling Laws for Stellarators

Different scalings for the global energy confinement time τ_E fit present stellarator data: (1) the Large Helical Device (LHD) scaling [31],

$$\tau_E^{LHD} = 0.17 R_0^{0.75} a_p^2 n^{0.69} B_0^{0.84} P^{-0.58} , \tag{2.4-1}$$

an empirical fit to stellarator data; (2) the gyro-reduced Bohm scaling [32],

$$\tau_E^{grB} = 0.25 R_0^{0.6} a_p^{2.4} B_0^{0.8} n^{0.6} P^{-0.6} , \tag{2.4-2}$$

which is based on drift-wave theory; and (3) the Lackner-Gottardi scaling [33],

$$\tau_E^{LG} = 0.17 R_0 a_p^2 n^{0.6} B_0^{0.8} P^{-0.6} \iota^{0.4} , \tag{2.4-3}$$

which fits both tokamak and stellarator data. Here B_0 is the on-axis field, n is the line-averaged electron density (in 10^{20} m^{-3}), a_p is the average radius of the noncircular (and nonaxisymmetric in stellarators) last closed magnetic surface, and P is the absorbed heating power (in MW). All other quantities are in SI units.

Unlike the LHD scaling, the Lackner-Gottardi scaling and the gyro-reduced Bohm scaling are dimensionally correct; that is, they are expressible in terms of dimensionless plasma parameters. In addition, they have the same functional dependence on the reactor parameters R_0, B_0, n, and P, differing only by an aspect-ratio-dependent coefficient. Coincidentally, the Lackner-Gottardi and LHD scalings also give nearly the same value of τ_E for typical reactor cases, even though they have different functional dependences on the reactor parameters.

Lackner-Gottardi scaling was monitored with a confinement improvement factor H' similar to the H-mode confinement improvement factor for tokamaks: $\tau_E = H' \tau_E^{LG}$. Evidence from experiments and theoretical arguments support such a confinement improvement. However, the improvement with the square root of the ion mass used in tokamak scaling is not assumed in our study, and ι is evaluated at a normalized radius $\rho = r/a_p = 2/3$, rather than at the plasma edge; incorporating the mass dependence, as is done in the Garching studies, would reduce the confinement multiplier needed by a factor of 1.3.

2.4.2. Comparison with Tokamak Scaling

Stellarators and tokamaks have similar energy confinement time scaling, indicating that the underlying physics may be dominated by common toroidal plasma physics rather than coil-geometry-specific effects. Figure 2.4-1 shows the measured energy confinement time τ_E versus that calculated for gyro-reduced Bohm scaling for different stellarators [34] and for the tokamak L-mode data base [35] where

$$\tau_E^{grB}(stell) \;=\; 0.25 B_0^{0.8} n^{0.6} P^{-0.6} a_p^{2.4} R_0^{0.6} A_i^{-0.2}\,, \tag{2.4-4}$$

for stellarators and

$$\tau_E^{grB}(tok) \;=\; 0.194 I_p^{0.8} n^{0.6} P^{-0.6} a^{2.2} R_0^{0.6} A_p^{1.02} A_i^{-0.2}\,, \tag{2.4-5}$$

for tokamaks using average tokamak quantities (plasma ellipticity $\kappa = 1.4$, average plasma aspect ratio $A_p = 3$, safety factor $q_{cyl} = 3$) to connect the tokamak plasma current I_p to the on-axis field B_0. Here a is the plasma minor radius (for tokamaks), and A_i is the average ion mass (= 2.5 for the D-T plasma).

Generally, confinement in stellarators is competitive with that in comparable tokamaks. However, present stellarators [2] are much smaller ($a_p = 0.2 - 0.27$ m) than present tokamaks ($a_p = 0.85 - 1.62$ m) and have not yet demonstrated adequate confinement and beta at parameters that can be extrapolated to the reactor regime. It is evident from Fig. 2.4-1 that the gap between the present performance and that needed for a practical power plant is much larger for stellarators than it is for tokamaks, typically, only 5-10 for tokamaks. Until larger ($a_p = 0.52 - 0.65$ m) next-generation stellarators [36, 37] begin operation near the end of this decade, assessment of the reactor potential of stellarators must rely on large extrapolations from present experiments and commonality with tokamak results.

2.4.3. Improvement in Confinement

Stellarators, like tokamaks, need to rely on an improved confinement regime for an attractive reactor. However, because of their larger plasma volume, stellarators do not require as large an improvement factor. For a confinement scaling law for which $\tau_E \propto P^{-0.6}$, which applies to both tokamaks and stellarators, a simple power balance argument shows that $\langle\beta\rangle \propto H^{2.5} P_E$ [38]. Beyond a certain point, an improvement in confinement must be accompanied by a corresponding improvement in the beta limit, or it cannot be used. Tokamaks typically require $H' \approx 2.5$ (as for ARIES-IV), but MHH only requires

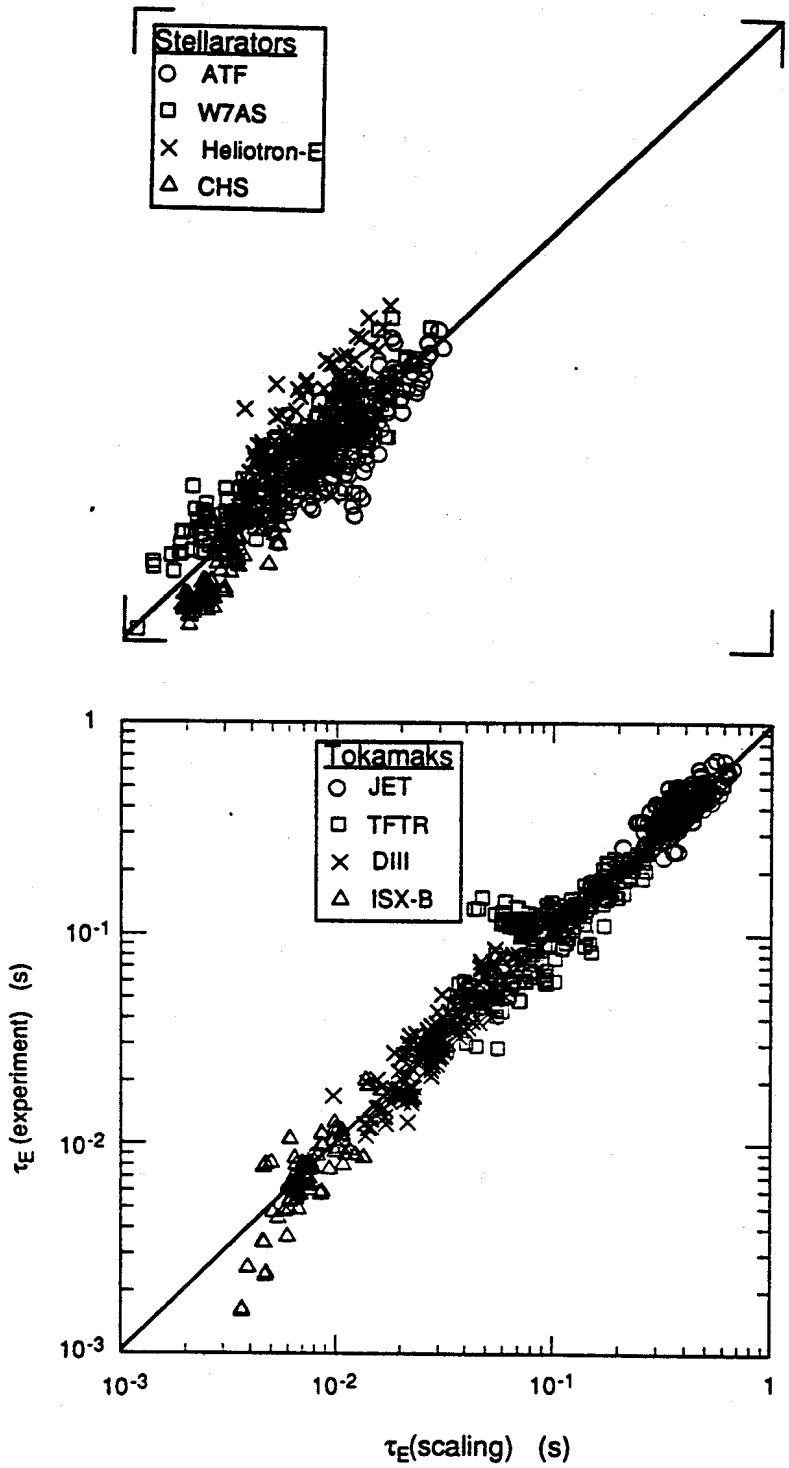

Figure 2.4-1. Energy confinement scaling for different stellarators and the tokamak L-mode database.

$H' \approx 1.5$. This is not too far from the confinement improvement seen in W7-AS ($H' \approx 1.3$) [39] and in CHS [40], but there is room for further improvement. The Pfirsch-Schlüter and bootstrap currents are reduced in the MHH configuration over those in present stellarators, so there is less free energy to drive instabilities. In addition, the effective helical ripple of the MHH configuration is reduced over that in a conventional stellarator because of MHH's quasi-helically symmetric features, so ripple-induced transport at low collisionality should also be reduced. A confinement improvement factor of $H' \approx 1.5$ appears to be reasonable, and the next-generation of stellarator experiments should aim at higher factors, similar to the goal of advanced tokamaks.

2.4.4. Density Limit

The maximum plasma density in stellarators is not determined by a disruption limit as in tokamaks. Sudo *et al.* [31], have proposed a maximum line-average density,

$$n_{max} = 0.25(PB_0/R_0 a_p^2)^{1/2} , \tag{2.4-6}$$

based on Heliotron E data. Densities a factor of 1.3 higher than this value have been observed in ATF. For this study, it is assumed that the line-average density is constrained to $< 1.5 n_{max}$.

2.4.5. Transport Modeling

Four different steady-state transport modeling approaches were used for the MHH power balance studies in the SPPS. Time-dependent calculations were not necessary because the time scale on which the plasma moves along a controlled operating path in the density-temperature plane is much longer than the energy confinement time (seconds) and other faster timescale phenomena (*e.g.,* tokamak "sawteeth") do not occur in stellarators. The main approach, that used in the ARIES studies and reported here, was 0-D calculations of $\langle T \rangle$ with fixed $n_e(r)$, $n_i(r)$, $T_e(r)$, and $T_\mathrm{i}(r)$ using the global Lackner-Gottardi τ_E scaling model [Eq. (2.4-3)]. Here $n_e(r)$ and $n_i(r)$ are the electron and ion density profiles with $n(r)$ parabolic, and $\langle T \rangle$ is the density-averaged plasma temperature with the electron and ion temperature profiles $T_e(r)$ and $T_i(r) \propto (\text{parabolic})^{1.1}$. Impurities are modeled by 1% C and 0.01% Fe. The helium ash accumulation and fuel ion dilution are calculated from the fusion reaction rate and an assumed value for the ratio of the helium particle confinement time τ_{He} to the energy confinement time τ_E at each value of $\langle n \rangle$ and $\langle T \rangle$.

Calculations using the other approaches are reported elsewhere: (a) 1-D calculations of $T_e(r)$ and $T_i(r)$ with fixed $n(r)$ and $\chi(r)$ normalized to the global Lackner-Gottardi τ_E scaling model [41]; (b) 1-D calculations of $T_e(r)$ and $T_\mathrm{i}(r)$ with fixed $n(r)$, $\chi_{anom}(r)$, and $E_r(r)$ with the Shaing-Houlberg ripple-induced neoclassical transport matrix [42]; and (c) 1-D self-consistent calculations of $T_e(r)$, $T_i(r)$, $n_e(r)$, $n_i(r)$, and $E_r(r)$ with fixed fueling profile for the Shaing-Houlberg ripple-induced neoclassical transport matrix and anomalous $\chi(r)$ and $D(r)$ [43]. Here $\chi(r)$ and $D(r)$ are the thermal and particle diffusivity profiles, and $E_r(r)$ is the radial electric field.

Figure 2.4-2 shows the operating space for an MHH reactor in the POPCON (Plasma OPerating CONtour) density-temperature ($\langle n\rangle - \langle T\rangle$) plane [44] with contours of the externally applied heating power P_{ext} required for equilibrium at a given point (the light solid curves labeled in MW from 0 to 100 MW in 10-MW intervals and in 100-MW intervals for auxiliary heating powers $\geq$ 100 MW). Contours of constant $\langle\beta\rangle$ (in multiples of 5%) and constant thermal fusion power (P_{fus}, in multiples of $P_{fus,op} = 1.73$ GW) are indicated by the dotted and chain-dash curves, respectively; $\langle n\rangle$ is the volume-averaged electron density. The ignition contour is the heavy curve where $P_{ext} = 0$. The dotted curve indicates the Sudo density "limit" calculated from Eq. (2.4-6). The reference assumptions in Fig. 2.4-2 are $R_0 = 14$ m, $a_p = 1.63$ m, $B_0 = 5$ T, $H' = 1.5$, $\tau_{He}/\tau_E = 6$, and 5% alpha-particle power lost.

The ignited MHH operating point, indicated by a "•", occurs where the $P_{fus,op} =$ 1.73 GW contour crosses the ignition curve. In Fig. 2.4-2, $P_{fus} = 1.73$ GW, corresponding to $P_E = 1$ GW for the values of thermal conversion efficiency and blanket energy multiplication assumed in the SPPS. The values obtained for the reference operating point are $\langle n\rangle = 1.24 \times 10^{20}$ m^{-3}, $\langle T\rangle = 11.5$ keV, $\langle\beta\rangle = 4.4\%$, $f_{He} = 5\%$, and $Z_{eff} = 1.46$. The values for P_{fus} and $\langle\beta\rangle$ vary as $\langle n\rangle$ and $\langle T\rangle$ vary along the ignition curve. The minimum values for the reference case in Fig. 2.4-2 are $P_{fus,min} = 0.69$ GW ($P_E = 0.4$ GW) and $\langle\beta\rangle_{min} = 2.69\%$.

The ignition contour in the POPCON plots, and consequently the operating point, varies with the MHH reactor parameters that are assumed. Figure 2.4-3 shows POPCON plots for six different values of the Lackner-Gottardi confinement multiplier, H'. The contour curves are characterized by the same values as in Fig. 2.4-2. As H' increases from 1.3 to 2, the operating point moves along the ignition curve from higher density and lower temperature to lower density and higher temperature. Actually, the constant-P_{fus} curve remains fixed and the ignition curve changes because P_{fus} is approximately proportional to $\langle n\rangle^2\langle T\rangle^2 R_0^3$. The constant-$\langle\beta\rangle$ curve also remains unchanged: $\langle\beta\rangle \propto \langle n\rangle\langle T\rangle/B_0^2$. As a result, the values of $P_{fus,min}$ and $\langle\beta\rangle_{min}$ along the ignition curve change as H' varies.

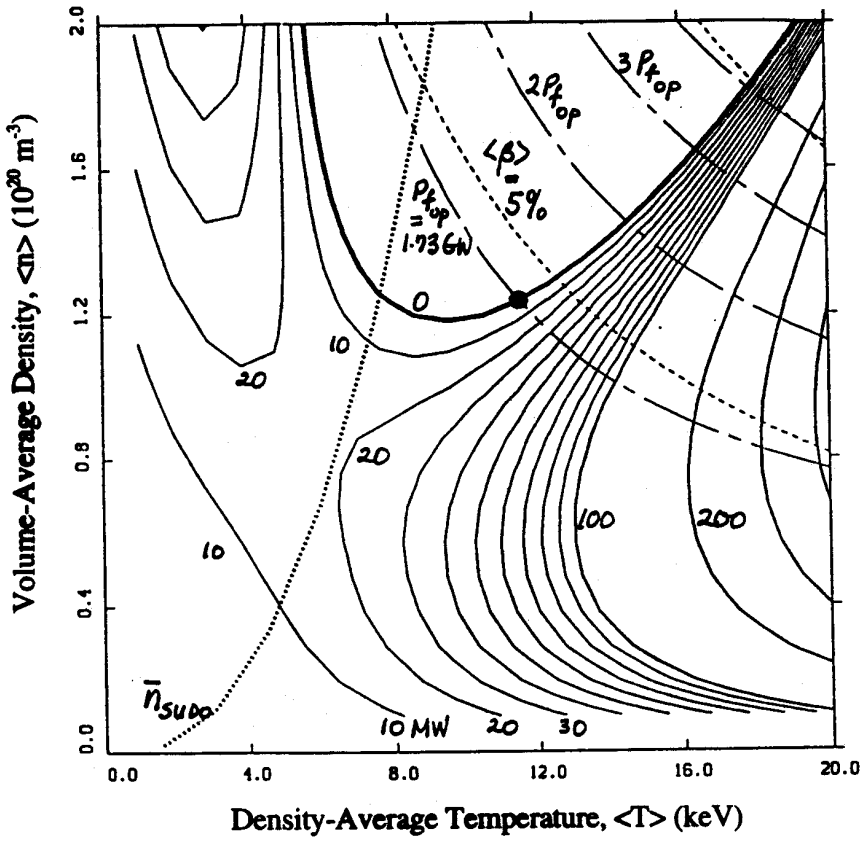

Figure 2.4-2. POPCON plot for the reference MHH power plant parameters: $R_0 = 14$ m, $B_0 = 5$ T, $\tau_{He}/\tau_E = 6$, and $H' = 1.5$.

Table 2.4-I summarizes these results as H' varies from 1.2 to 2. The operating point is thermally stable to small excursions in $\langle n \rangle$ and $\langle T \rangle$ on the right branch of the ignition curve (where $\partial\langle n \rangle/\partial\langle T \rangle > 0$). This occurs for $H' > 1.35$. The operating point is thermally unstable for lower values of H'. An operating point with $P_{fus} = 1.73$ GW cannot be obtained for $H' < 1.245$ where $P_{fus,min} > 1.73$ GW. Figure 2.4-4 shows the POPCON curves for the minimum value ($H' = 1.245$) that satisfies the constraint that an ignited operating point exist with $P_{fus,op} = 1.73$ GW. The $P_{fus,op} = 1.73$ GW contour does not intersect the ignition curve for lower values of H'.

Unlike tokamaks, stellarators do not require power input to the plasma once the self-heating from fusion-produced alpha particles dominates the power balance; at this point the plasma runs away to ignition. In the POPCON plots, this occurs where $\partial P_{ext}/\partial\langle T \rangle < 0$; *i.e.*, along a curve that connects the minima of the P_{ext} contours. The most efficient

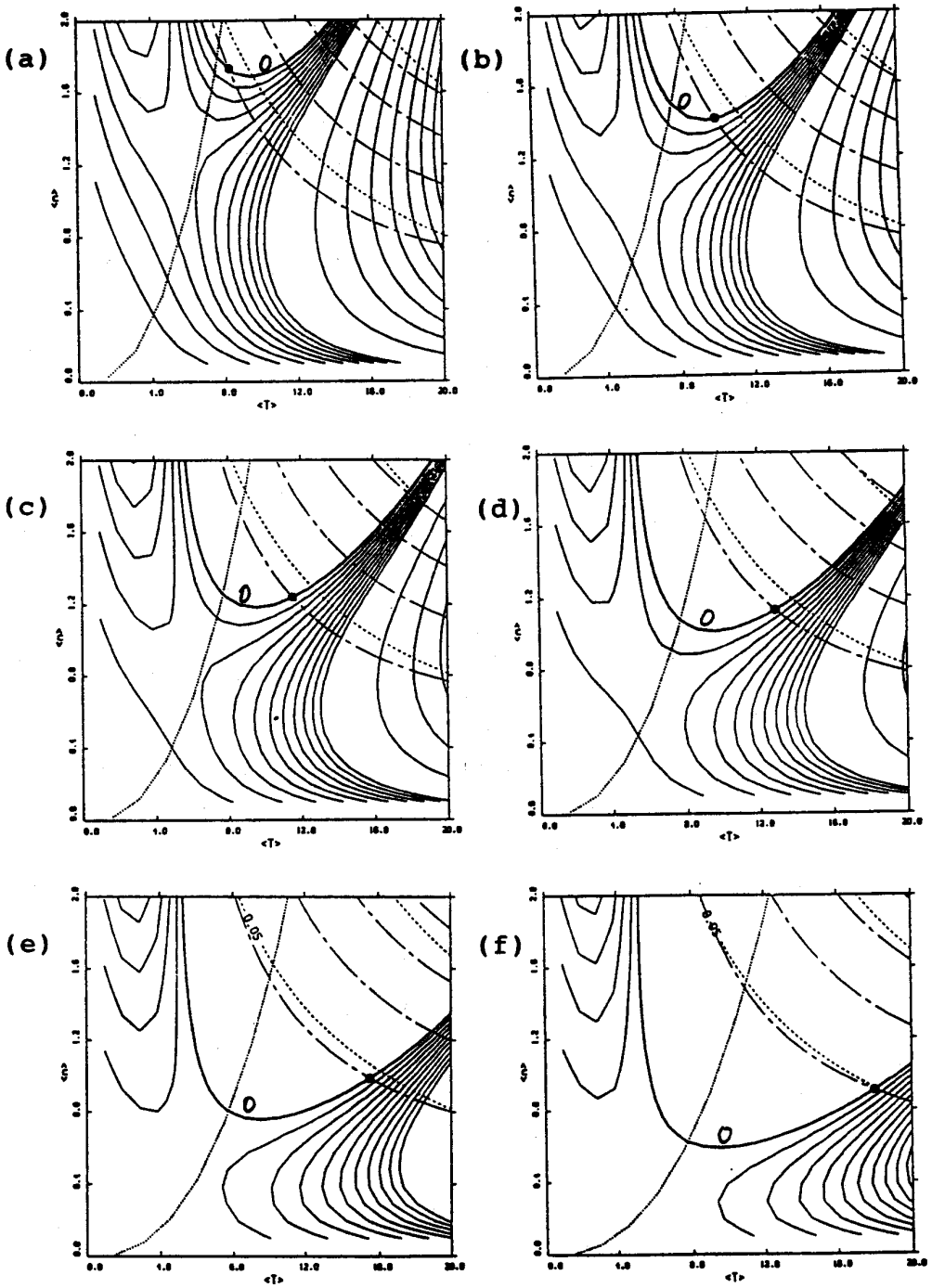

Figure 2.4-3. Movement of ignition contour and operating point with confinement improvement factor H': (a) $H' = 1.3$, (b) $H' = 1.4$, (c) $H' = 1.5$, (d) $H' = 1.6$, (e) $H' = 1.8$, (f) $H' = 2$.

Table 2.4-I.
MHH Reactor Parameters for Different H' Assumptions with $\tau_{He}/\tau_E = 6$

H'_{L-G}	f_{He}	$\langle n \rangle$ (m^{-3})	$\langle T \rangle$ (keV)	$\langle \beta \rangle$	$P_{fus,min}$ (GW)	$\langle \beta_{min} \rangle$	P_{SP} (MW)
1.2	—	—	—	—	2.06	5.11%	55
1.25	3.7%	2.19×10^{20}	6.9	4.65%	1.69	4.65%	45
1.3	4.0%	1.73×10^{20}	8.3	4.44%	1.52	4.24%	37
1.4	4.4%	1.41×10^{20}	10.0	4.35%	0.96	3.51%	25
1.5	5.0%	1.24×10^{20}	11.5	4.37%	0.69	2.96%	18
1.6	5.4%	1.13×10^{20}	12.9	4.44%	0.50	2.53%	13
1.8	6.4%	0.99×10^{20}	15.5	4.65%	0.28	1.90%	8
2.0	7.4%	0.91×10^{20}	18.0	4.93%	0.17	1.47%	5

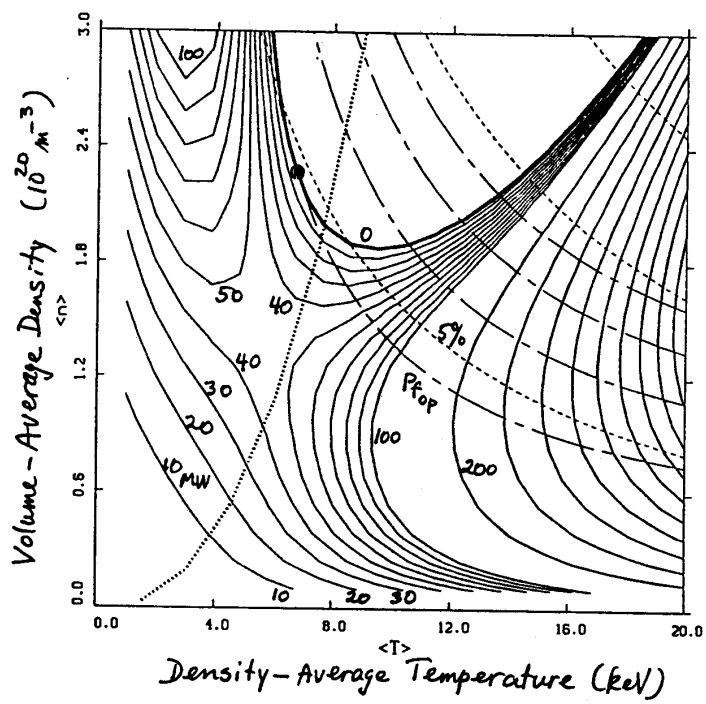

Figure 2.4-4. POPCON plot for the reference MHH power plant with $H' = 1.245$.

startup path passes through the minimum value of P_{ext} (P_{SP}) along this curve. This saddle point in the auxiliary heating power curves is the lowest value needed to reach ignition; it is listed in Table 2.4-I for different H' values. Below the saddle point in the $\langle n \rangle - \langle T \rangle$ plane, the operating path can be carefully controlled by controlling the density and the external heating power to allow a slow startup in which the plasma-facing components and blanket have time to come to thermal equilibrium. As the external power input is reduced above the saddle point, additional losses (either through additional impurity radiation or a perturbing magnetic field) are needed to slow the plasma evolution to ignition or to operate at reduced fusion power. One contributing factor that slows this path to ignition and reduces the additional losses needed for control is the buildup of helium ash, which increases the bremsstrahlung radiation and dilutes the D-T fuel density (see Table 2.4-II).

Since $P_{fus,min} = 0.69$ GW $< P_{fus,op} = 1.73$ GW for the reference case, it is possible to have MHH reactors with P_E down to 0.4 GW without changing the value for R_0 or B_0. The desired power level is controlled through the value of $\langle n \rangle$ on the ignition curve. Table 2.4-III shows the variation of the reference MHH reactor parameters as P_E varies from 0.5 GW to 2 GW. Here $\Gamma_{\rm n}$ is the average neutron wall loading. Although the cost of the reactor core would not change with P_E, the cost of electricity would decrease

Table 2.4-II.
MHH Reactor Parameters for Different τ_{He}/τ_E Assumptions with $H' = 1.5$

τ_{He}/τ_E	f_{He}	$\langle n \rangle$ (m^{-3})	$\langle T \rangle$ (keV)	$\langle \beta \rangle$	$P_{fus,min}$ (GW)	$\langle \beta_{min} \rangle$	P_{SP} (MW)
2	1.7%	1.12×10^{20}	11.8	4.12%	0.60	2.64%	17
4	3.3%	1.18×10^{20}	11.7	4.24%	0.63	2.79%	18
6	5.0%	1.24×10^{20}	11.5	4.37%	0.69	2.96%	18
8	6.6%	1.31×10^{20}	11.3	4.51%	0.76	3.15%	19
10	8.2%	1.40×10^{20}	11.1	4.65%	0.86	3.38%	20
12	9.8%	1.50×10^{20}	10.7	4.82%	0.97	3.68%	21
15	12.2%	1.71×10^{20}	10.1	5.11%	1.31	4.45%	22

Table 2.4-III.
MHH Operating Parameters for Different Values of P_E

P_E (GW)	$\langle n \rangle$ (m^{-3})	$\langle T \rangle$ (keV)	$\langle \beta \rangle$	f_{He}	Γ_n MW/m^2
0.5	1.21×10^{20}	8.4	3.13%	3.98%	0.52
0.6	1.19×10^{20}	9.3	3.39%	4.22%	0.62
0.7	1.19×10^{20}	10.0	3.64%	4.43%	0.73
0.8	1.20×10^{20}	10.6	3.89%	4.62%	0.83
1.0	1.24×10^{20}	11.5	4.37%	4.95%	1.04
1.25	1.29×10^{20}	12.5	4.93%	5.29%	1.30
1.5	1.35×10^{20}	13.3	5.47%	5.58%	1.56
1.75	1.40×10^{20}	14.0	5.97%	5.82%	1.82
2.0	1.45×10^{20}	14.6	6.45%	6.04%	2.08

significantly with increasing power output. Nevertheless, 1 GW(electric) was chosen to allow comparison with tokamak reactors. If the $\langle \beta \rangle$ value is limited to $< 5\%$, then a slightly larger value of R_0 or B_0 would be needed: $B_0^4 R_0^3 \propto P_E / \langle \beta \rangle^2$.

2.4.6. Plasma Heating Options

Different heating options are available for MHH power plant startup because external power input is only required transiently for plasma heating and not continuously for current drive. This power is only needed until the plasma is ignited, so it can be discontinued afterwards. The various options are electron cyclotron heating (ECH), ion cyclotron heating (ICH), and neutral beam injection (NBI). ECH is the preferred heating option because it can be located remotely from the plasma and connected to it via relatively small quasi-optical waveguides, minimizing the real estate needed for this system. The 280-GHz frequency required for second harmonic X-mode ECH at $B_0 = 5$ T allows

operation up to $n_e = 2.5 \times 10^{20}$ m^{-3}, above the required operating-point density. ICH is not as practical because it requires a larger launcher exposed to the plasma. NBI introduces a particle and momentum source in addition to heating the plasma and requires larger access to the plasma with the source components exposed to the intense neutron flux from the plasma during heating to ignition.

2.5. PARTICLE AND HEAT REMOVAL

2.5.1. Separation of Particle and Heat Removal

The fusion power is carried by alpha particles (with energy $E_\alpha = 3.5$ MeV) and neutrons ($E_n = 14.1$ MeV). The neutron flux is assumed to penetrate the first wall to be absorbed in the blanket and shield, so the only power impacting on the first wall and divertor is that which originates in the alpha particles. If the total fusion power is $P_{fus} = 1.725$ GW and the power limit on the divertor targets,Q_d, is 5 MW/m^2, then the surface area required for the divertor plates (if all the power is handled by the divertor) is

$$S = [E_\alpha/(E_\alpha + E_n)] \times [P_{fus}/Q_d] = 69\ m^2\ , \tag{2.5-1}$$

which is about 5% of the plasma surface area (1233 m^2). In the SPPS study, the divertor takes up about 15% of the plasma surface area, or about 185 m^2, so in principle a factor of 2.7 margin exists. However, the exiting flux is quite non-uniform around the torus and the power is not uniformly distributed on the divertor plates, so it is prudent to adopt some additional strategy to ensure engineering feasibility.

It would be useful to spread out the alpha-particle heat load over the entire first wall by radiating away most of the power at the edge. Experiments in the TEXTOR [45] and TORE SUPRA [46] tokamaks show that > 80% of the power can be converted to radiation by introducing a layer of impurities (*e.g.*, neon) at the plasma edge. It is assumed that this technique can be used for MHH, and that 80% of the power can be radiated to the wall (with an average power of 0.26 MW/m^2, a factor of 2 below the 0.5 MW/m^2 power-handling capability assumed for the first wall). The remaining 20% of the escaping alpha-particle power must be handled by the divertor, about 68 MW.

The particle flux calculation is more speculative because of the uncertainty in the value of the particle confinement time, τ_p. In the SPPS study, it is assumed that $\tau_p \sim 6\tau_E$. In most tokamaks, $\tau_p \sim 2\tau_E$. In elm-free H-mode tokamak plasmas, $\tau_p \sim 4\tau_E$. In some

experiments [47] in the ATF torsatron at Oak Ridge National Laboratory, biasing the edge of the plasma made $\tau_p >> \tau_E$. In steady-state, of course, the efflux of particles, Γ_p, times the area of the LCFS must equal the fueling rate, Φ(particles/second). The total number of particles in the plasma N_{tot} is given by the average density times the plasma volume, so

$$N_{tot}/\tau_p \;=\; (particles\, escaping/second) \;=\; \Phi/(1-R) \qquad (2.5\text{-}2)$$

where R is the recycling coefficient for particles at the plasma edge.

In divertor tokamaks, such as DIII-D, the recycling coefficient can be close to zero – most of the escaping particles go into the divertor, and very few make it back to the plasma. In pump limiters, typically 90% of the flux hits the limiter head and 10% goes into the divertor chamber. Of this 10%, about half may make it back into the plasma, so that R is about 0.95. The divertor geometry in the MHH stellarator is a sort of hybrid between a divertor and a pump limiter, so a wide range of values for R could occur.

2.5.2. Magnetic Geometry and Islands

The NESCOIL code can be used to create configurations with the same LCFS, but which can have quite different properties in the region between the LCFS and the CWS. This is accomplished by making small changes in the shape (Fourier harmonics) of the CWS.

The reference MHH has small $n/m = 4/3$ islands outside of the LCFS. These islands actually change the shape of the LCFS slightly. There are also variations of the MHH configuration with large islands surrounded by good closed flux surfaces, and configurations in which this outer region is very chaotic. This flexibility offers many options in designing the divertor geometry.

For example, one variation (Fig. 2.5-1) shows a version of MHH (normalized to $R_0 = 10$ m) with large well-formed islands that are surrounded by non-ergodic closed flux surfaces. This sort of topology is well-suited to be used by a local island divertor (LID) [48], which is an extended form of a pumped limiter. The head of the divertor is placed within the island (the black cresent-shaped region in Fig 2.5-2). The back of the island intersects the back of the LID head (the gray region in Fig. 2.5-2) at a grazing incidence to spread the heat flux, and a second plate can be placed just outside of the outer LCFS to close off the pumping region.

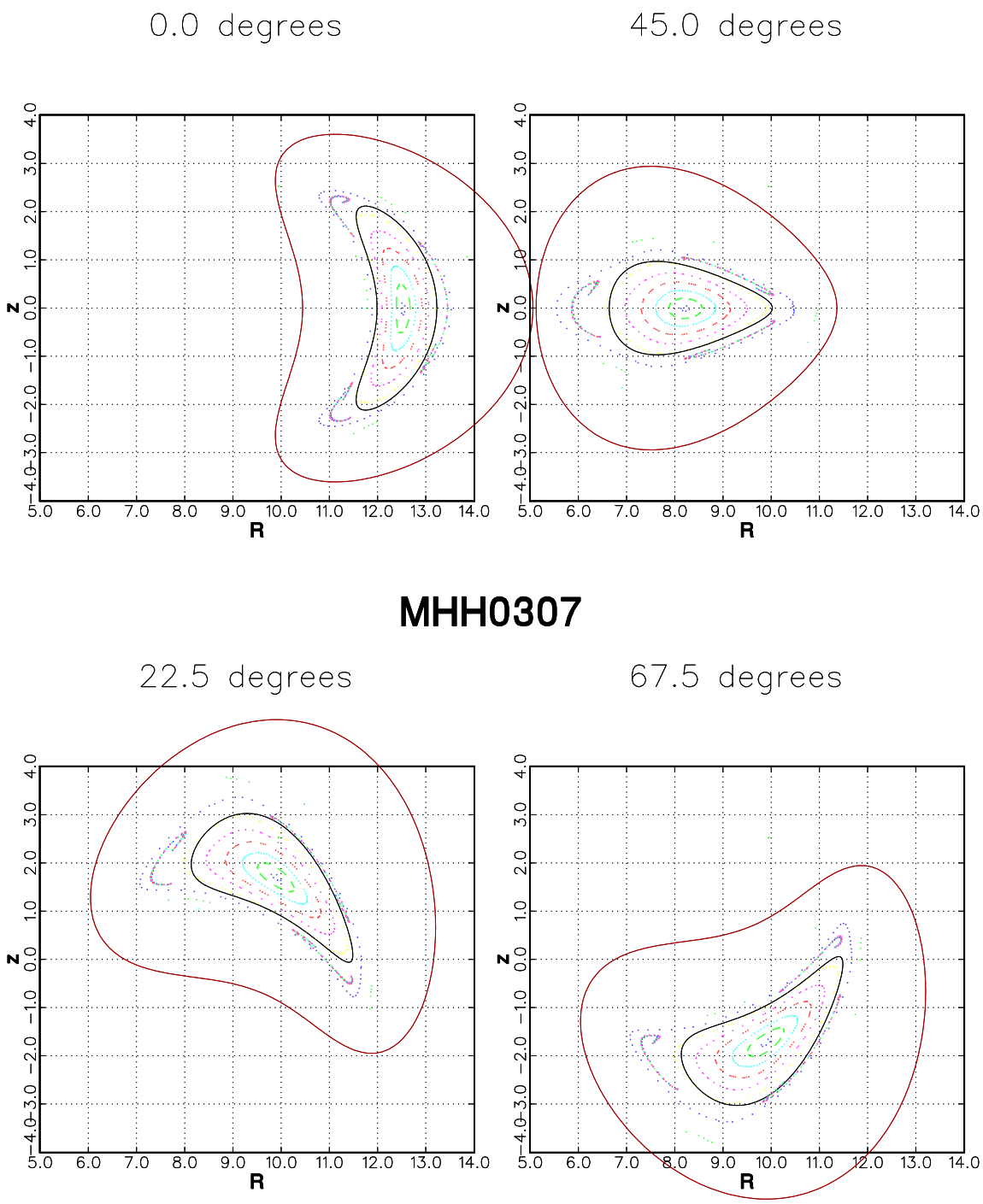

Figure 2.5-1. Cross section of magnetic surfaces (dotted), the nominal plasma boundary or LCFS (inner solid curve), islands (dotted) outside the LCFS, and the CWS (outer solid curve) at four toroidal angles in a field period.

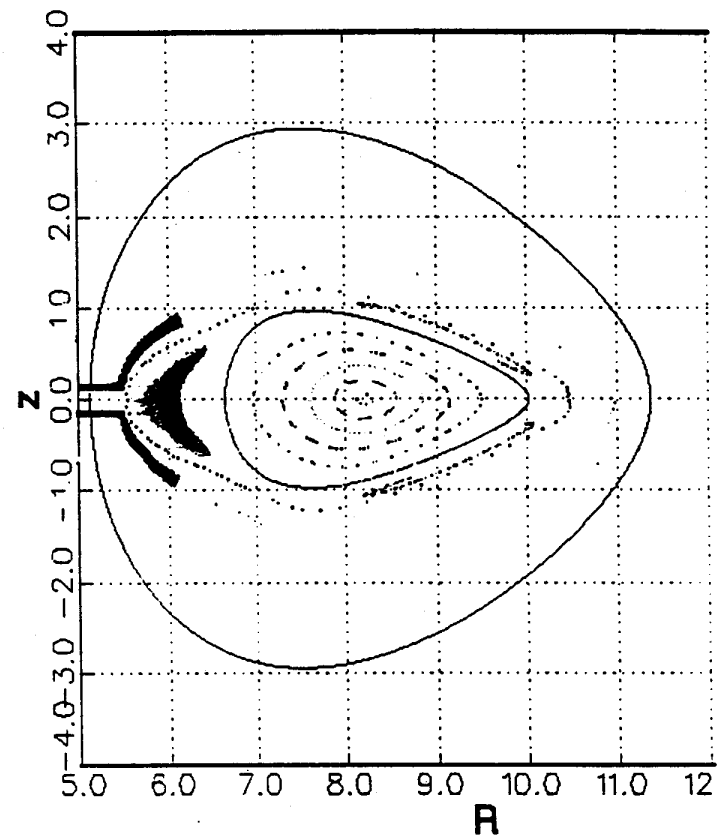

Figure 2.5-2. A rough drawing of a local island divertor configuration. The front of the head (black) is shielded from the flux. The back of the head (gray) is hit by the flux coming around the back of the island at a low angle of incidence.

The LID concept is being tested in the Japanese helical devices CHS and LHD. However, the operational configuration must be prespecified so that the LID will fit into the island at the operational conditions. As the plasma beta increases, the configuration might change if the Pfirsch-Schlüter and bootstrap currents do not remain at negligible levels. However, for the helias-like configuration of MHH, these currents are controlled, and the concept may be feasible.

A second option for MHH is to utilize the escaping flux bundles in multiple bundle divertors. This concept was explored in the Interchangeable Modular Stellarator at the University of Wisconsin in Madison. By biasing a plate in one of the escaping flux bundles, the flux can be transferred to a different bundle. This is important since it is impractical to collect all of the flux bundles. The advantage of the bundle divertor

approach is that the collector can be outside of the machine (past the modular coils). However, the channel for the escaping flux must be shielded on all sides, and these large orifices take away room for the blanket. Therefore, the bundle divertor approach may not be appropriate for MHH.

Instead, the MHH design uses the approach proposed by Garching for the W7-X helias. The islands outside the LCFS are used to solve the leading edge problem without inserting a plate entirely within the island. The island structure of MHH (with major radius here normalized to 9 m) is shown in Fig. 2.5-3. Instead of inserting the entire divertor plate within the island, the center of the plate is inside the island, and the edges of the plate (outside the island) are bent back so that they intercept the flux at the desired angle, as shown in Fig. 2.5-4. The big advantage of this scheme is that the island can move and change shape without major changes in the divertor operation. Indeed, the island surfaces can be slightly 'fuzzy' because the underlying connectivity topology remains even if the islands are somewhat broken up. The details of this design will be discussed in the next section.

The chief potential disadvantage of this approach is that by using divertor plates close to the plasma, it is difficult to create a closed geometry that can be plugged by a plasma and pumped. The pump location is behind the divertor plates, so either the plates must be slotted, or the neutralized plasma must find its way around the plates to the pumps.

2.5.3. Divertor Geometry

One way of assessing the geometry of the divertor region is to calculate the connection length of the field lines outside of the LCFS, the distance along a field line from that point to the divertor plate. In general, the field lines that go close to the LCFS and that have a long connection length to the divertor plate will carry the most plasma particles. To calculate the connection length topology, the region between the LCFS and the CWS was divided into concentric shells. Field lines were launched on each shell headed towards the plasma. For each field line, the minimum distance to the plasma and the distance to the birth surface (twice the connection length) were calculated. Fortunately, the connection length is maximized for those field lines that approach closest to the LCFS because these field lines go around the outside of the islands or their remnants.

Figure 2.5-5 shows one way of displaying this information. Magnetic field lines are launched on a $\theta - \phi$ grid on the phantom surface that is 20% of the way out from the LCFS to the CWS. Note that the angle θ is the one used in the parameterization of the

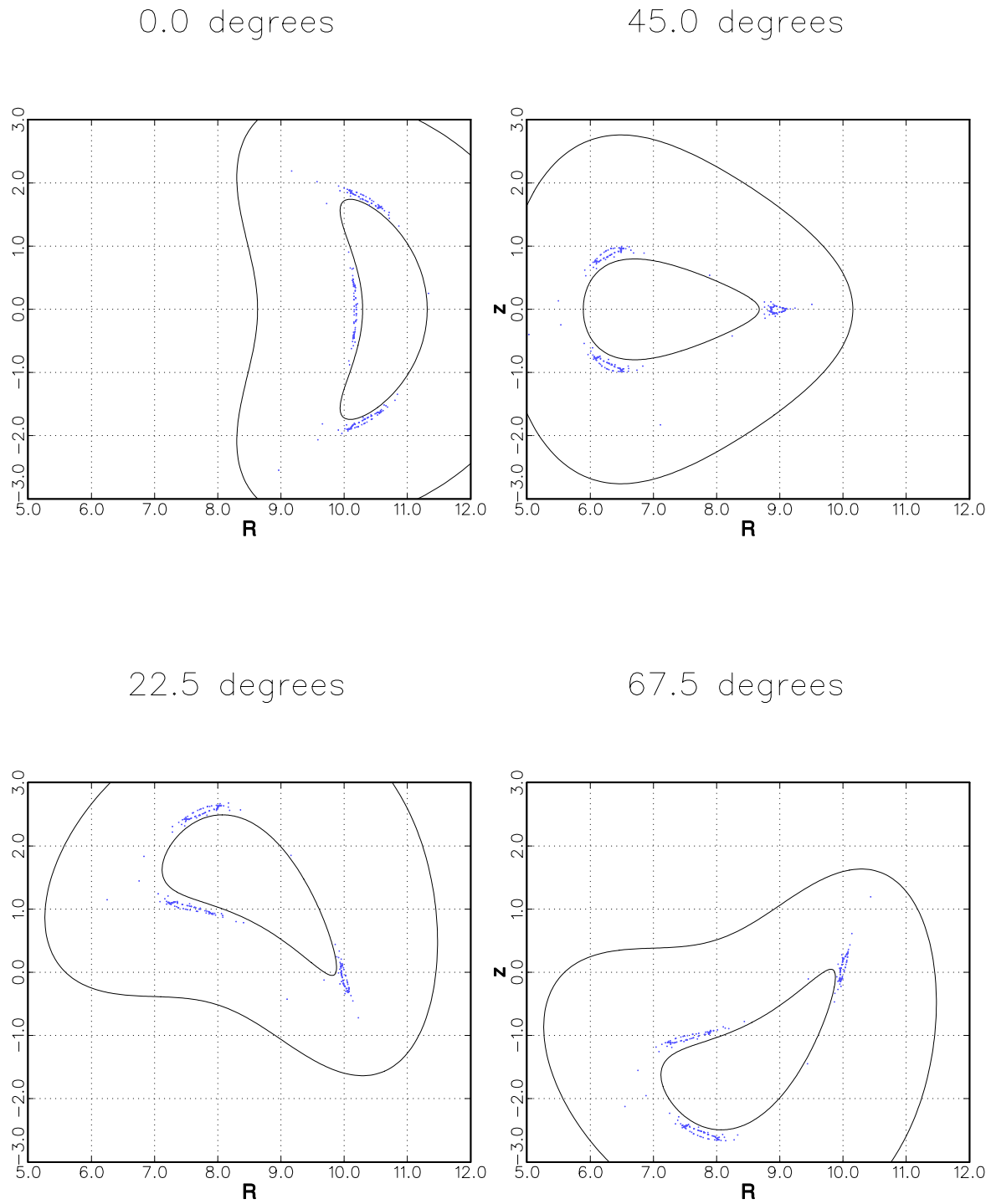

Figure 2.5-3. The island structure for the base case of MHH. This particular example has been scaled for a 9-m average major radius.

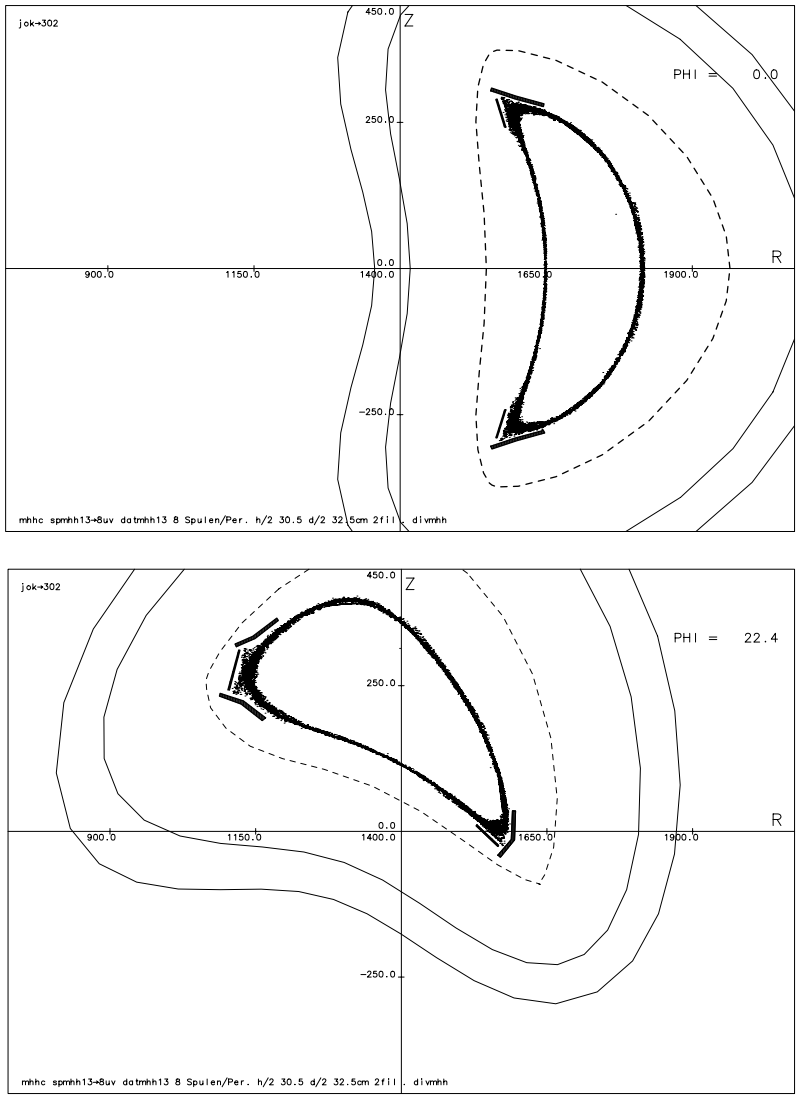

Figure 2.5-4. Cross section of the last magnetic surface and the coil boundary at $\phi = 0°$ (top) and $\phi = 22.5°$ (bottom) indicating the divertor plate scheme proposed for MHH. Diffusion of field lines outside the last closed magnetic surface is shown in the vicinity of the divertor targets (thicker black objects) and the baffle plates (thinner black objects) at the apexes of the MHH configuration. The dotted curve indicates a 2-m distance from the coil boundary.

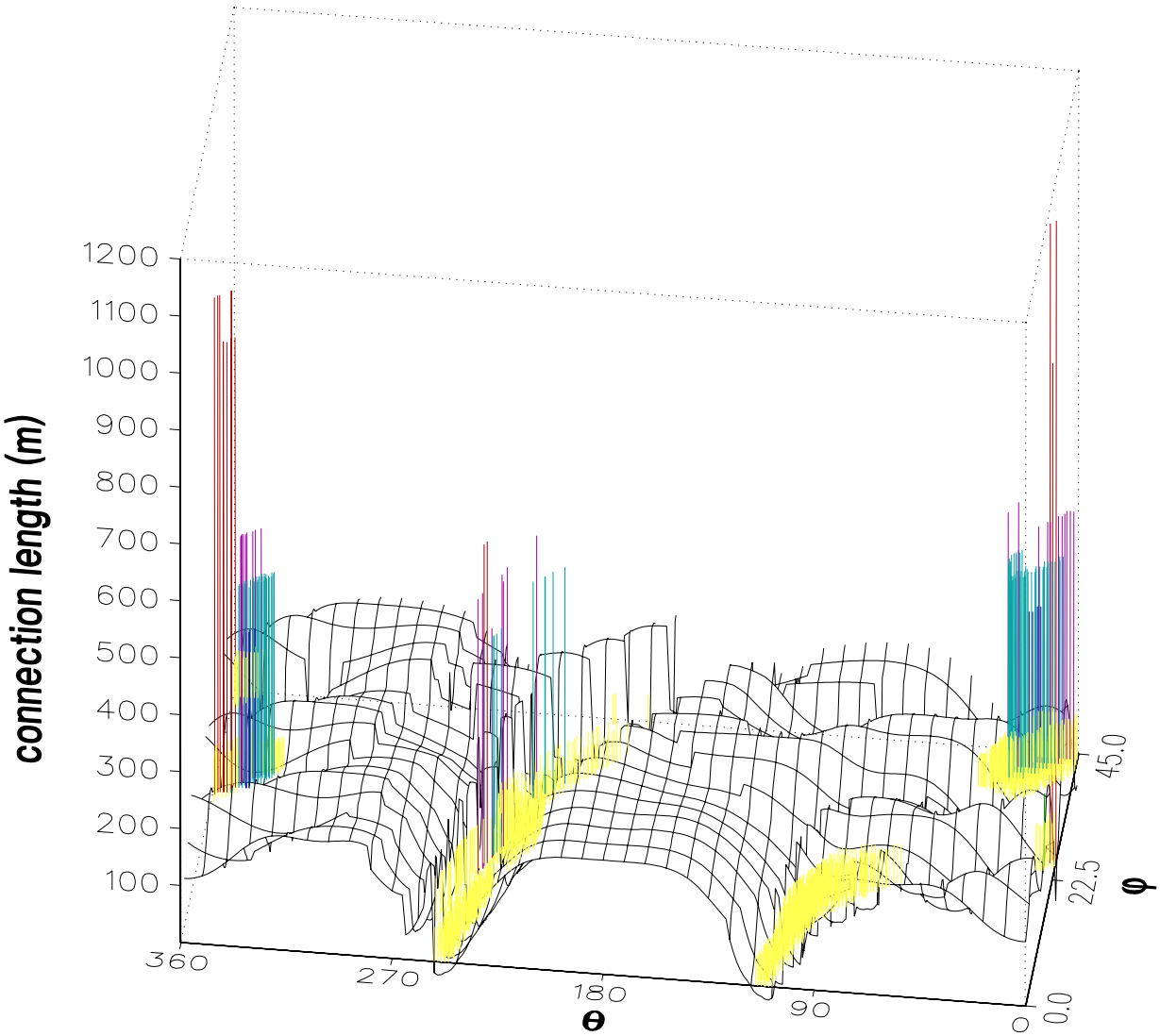

Figure 2.5-5. Field lines are launched from a θ-ϕ grid located on a phantom surface 20% of the way from the LCFS to the CWS. The 3-D surface represents the distance of closest approach of each field line to the LCFS and the lines represent the lengths of the field lines.

surface. A $\theta =$ constant line rotates helically and returns to its original position after one field period. In this plot, the connection length is defined as the total length of the field line from the starting point until it returns to the launch surface. The field lines with connection lengths above 50 m are shown as vertical lines whose height is proportional to the connection length. Each line is plotted twice – at both the starting and ending values of θ and ϕ. On the same plot, the wire-frame grid represents the distance of closest approach of the field line to the LCFS. Actually, the minimum value of the flux is plotted, so the height of this surface can go slightly negative because of the small 4/3 island chain outside the LCFS. The important point to note is that the long connection-length field lines (the spikes) also approach closest to the plasma, *i.e.,* they occur in the troughs of the wire-frame surface. Figures 2.5-6 and 2.5-7 show the same plot for launch points 10% and 15% of the way out from the LCFS to the CWS. The coincidence of the long connection lengths and close approach to the plasma is repeated on these surfaces also. However, the $\theta - \phi$ locations of the longest field lines change. Puncture plots of the long-connection-length field lines that were launched 25% of the way out from the LCFS to the CWS (shown in Fig. 2.5-8) show how the islands corral the exiting flux so that it goes around the islands rather than through them.

The converse problem has also been solved by the Garching group for W7-X. Starting at the plasma and work outwards, the regions of increasing field line connection length are nested, with the longest being just outside of the LCFS. This nesting is especially striking in the vicinity of the X-points at the tips of the bean-shaped cross-section.

Much of the MHH divertor design has been performed by the W7-X group [49]. Their approach to the problem is as follows:

1. determine the exact position of the separatrix, especially the X-points, and find the size of the $\iota = 4/3$ islands outside of the last closed flux surface;
2. investigate the field stucture outside the last closed surface;
3. choose the poloidal and toroidal position of segmented target and baffle plates, with planar surface elements, in regions where the islands have a large radial extension and provide enough space towards the first wall;
4. adjust the minor radius position of the target plates for field line intersection angles of about 1° to 2°;
5. follow magnetic field lines (with an additional artificial diffusion) that are started inside the LCFS until they intersect the plates;

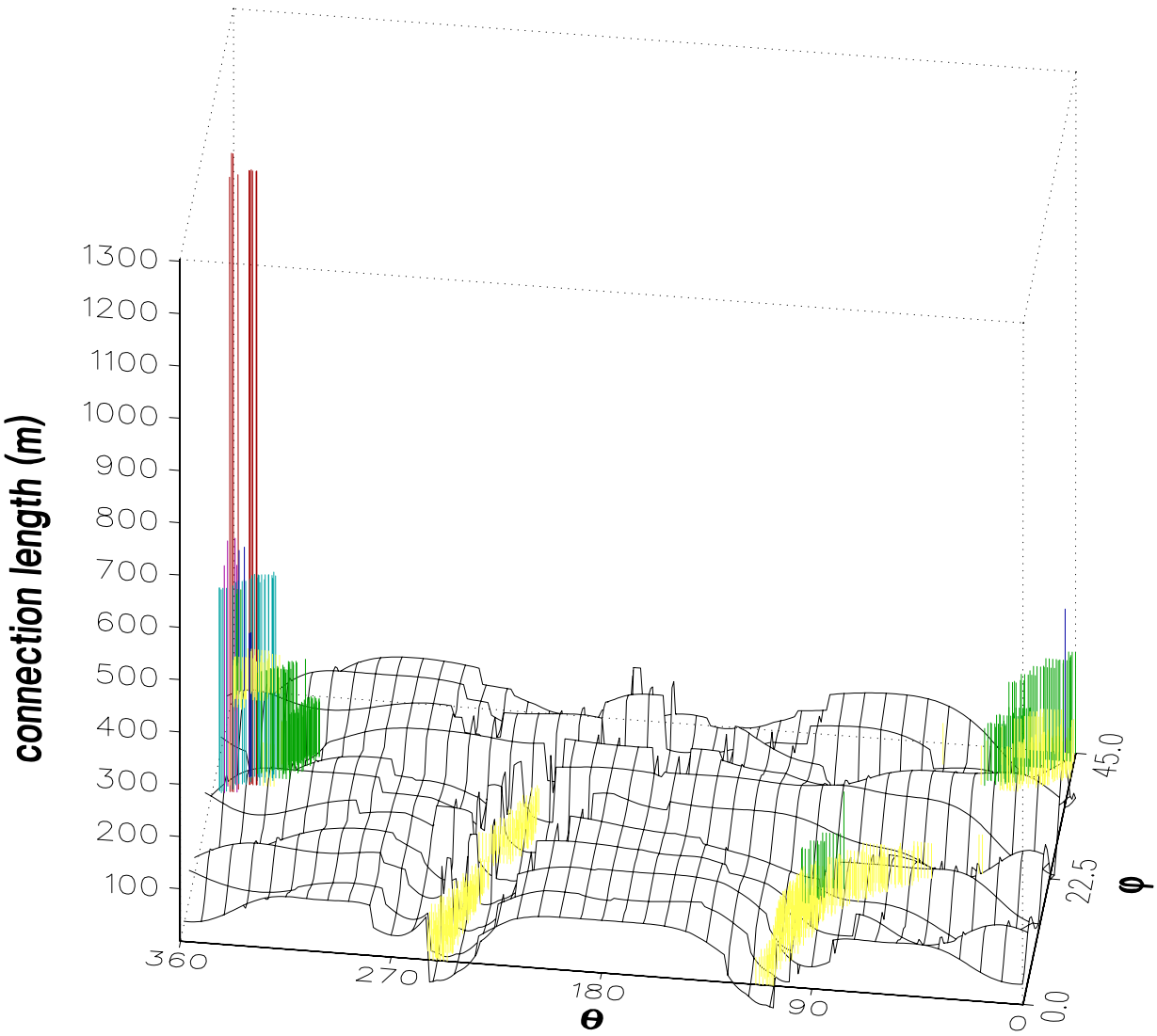

Figure 2.5-6. The same plot as in Fig. 2.5-5, but for field lines launched 10% of the way out from the LCFS to the CWS.

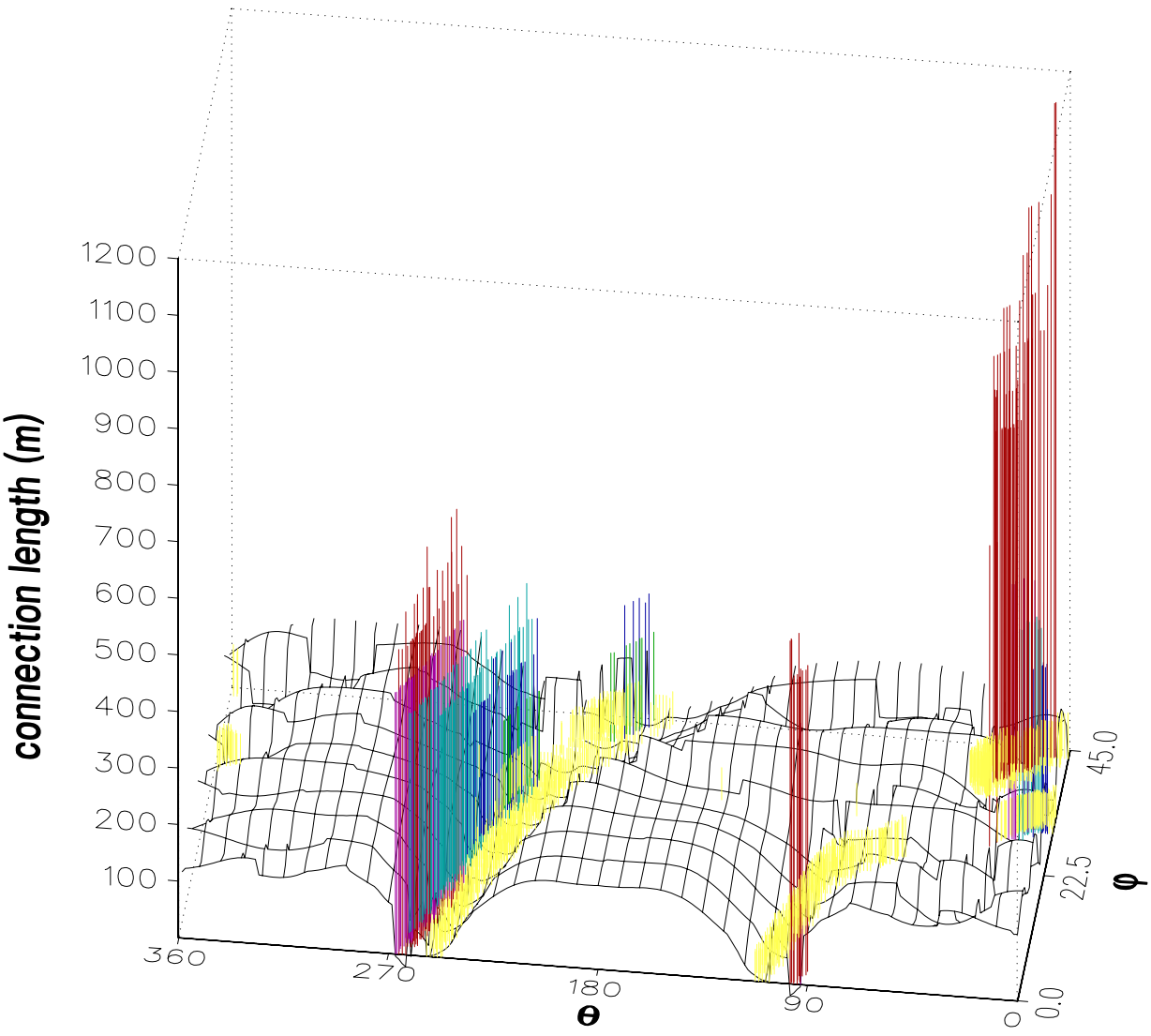

Figure 2.5-7. The same plot as in Fig. 2.5-5, but for field lines launched 15% of the way out from the LCFS to the CWS.

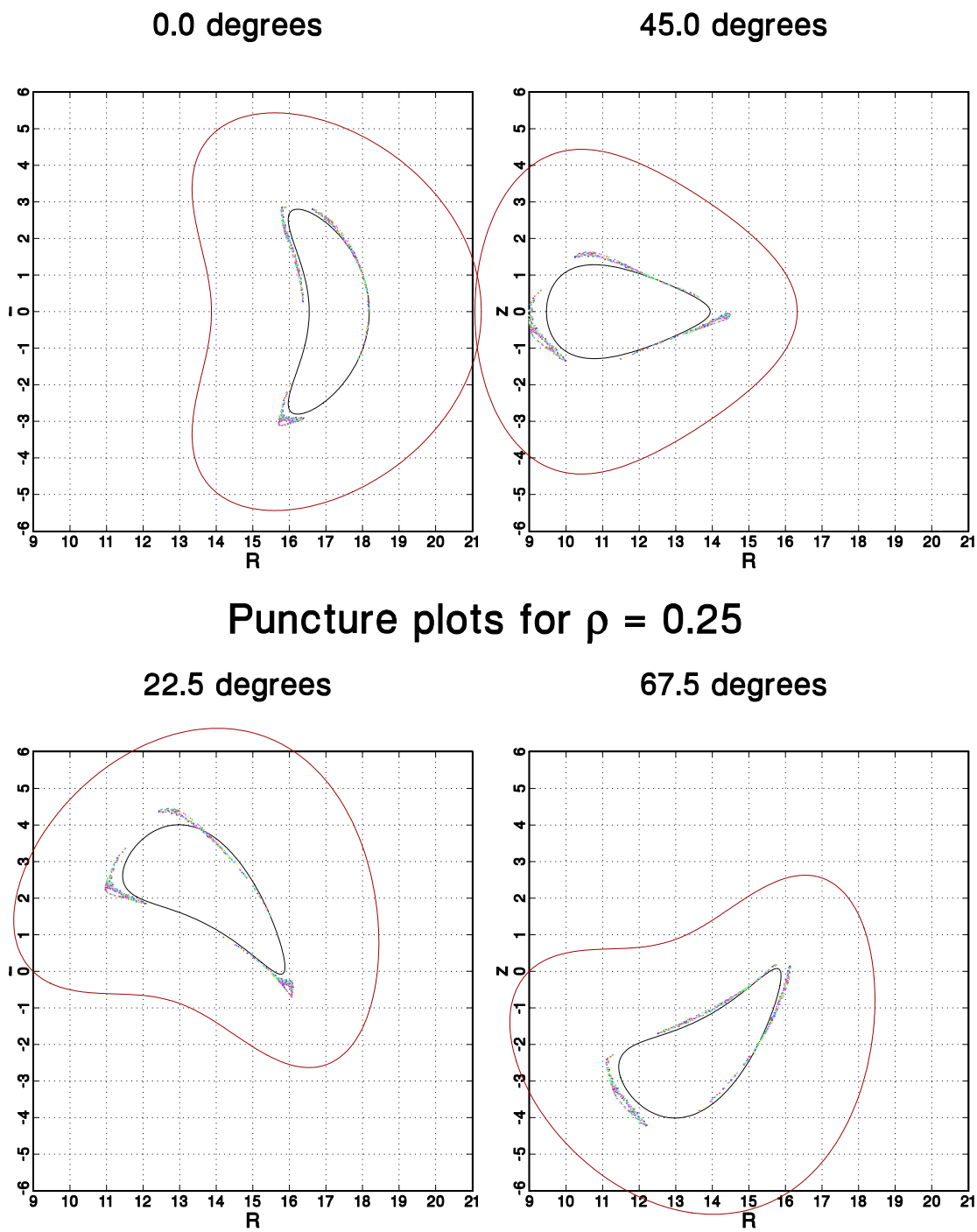

Figure 2.5-8. Puncture plots of the long connection length field lines launched on a grid that is 25% of the way out from the LCFS to the CWS. This plot illustrates how the presence of the small islands corrals the exiting flux.

6. improve the size and position of the plates in a number of iterations with the preceding step, and verify that local high power loads are avoided, especially at the 'leading edges'; and thus

7. arrive at an interim solution, as shown in Fig. 2.5-9 [24], with a power loading given by the deposition pattern at the target plates.

For this rather quick study, a coarse segmentation of the target plates was used. Thus the intersection pattern is not uniform, but the 'leading edge' problem is definitely avoided. The target and baffle plates for MHH are in the toroidal region near the apexes of the bean-shaped cross section, as is the choice for the W7-X divertor configuration.

Four different variations of the base case were examined [24], labeled MHH-A, MHH-B, MHH-C, and MHH-D. The configuration MHH-A was selected as the SPPS base case. These cases differ in the current density and cross-section of the modular coils. There are only minor differences between the edge structures of the four data sets, regarding the position and size of the last closed surface or of the $\iota = 4/3$ islands. MHH-B does not have space for a divertor if a uniform radial width of 1.3 m is assumed between the bore of the winding pack and the LCFS. The distance between the LCFS and the coil bore is larger for MHH-C than for MHH-A, due to the different position of the winding pack bores. MHH-D with the smallest radial thickness of the winding pack does not improve the spatial situation regarding a divertor, but has rather large forces because of a very high current density (50 MA/m^2) in the winding pack. Reacting these very large forces and torques may lead to unworkably large support structures.

Two main problems exist with the MHH divertor configuration, namely the rather small radial island thickness and the tightness of the distance between the first wall and the last closed surface, especially at the inboard side in the middle of a field period (at the triangular cross section). The edge flux surfaces have a bulge in this region, shown in Fig. 2.2-3, which is caused by the presence of the X-point of the $\iota = 4/3$ islands. This bulge is enhanced if the number of coils per period is reduced. In order to develop our present interim solution towards a more useful divertor for MHH, new coils with improved shapes need to be defined using the NESCOIL code. The lateral width and the radial coil height then can be optimized for given values of the axis and peak magnetic fields, the coil current density, and the required radial and lateral coil support. The first problem of an increased radial island size can be solved by redefining the current winding surface via an iterative 'fine-tuning' of the numerical NESCOIL output, with magnetic field line tracing in order to maintain the properties of the configuration. Obviously, further

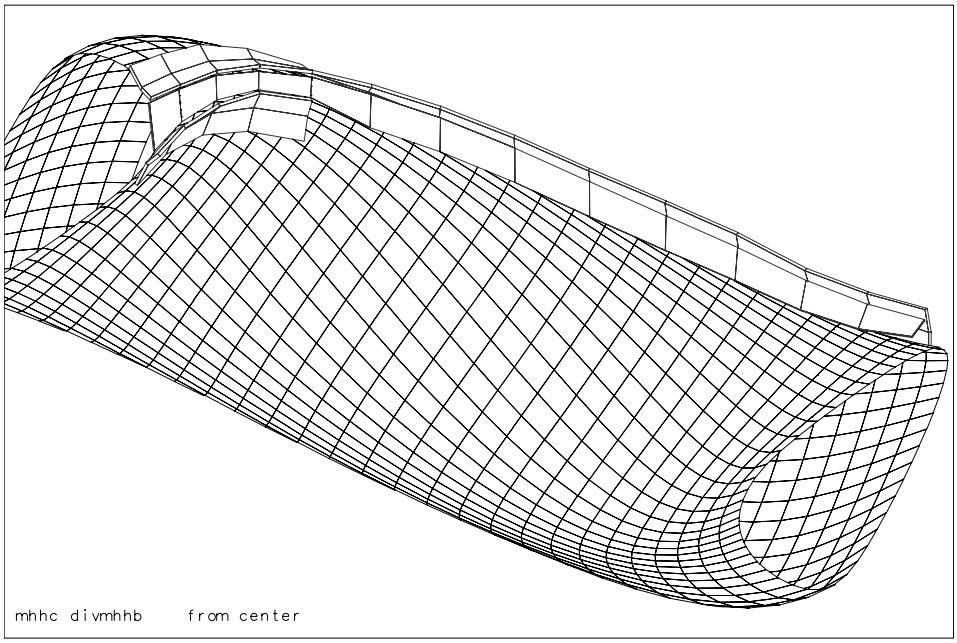

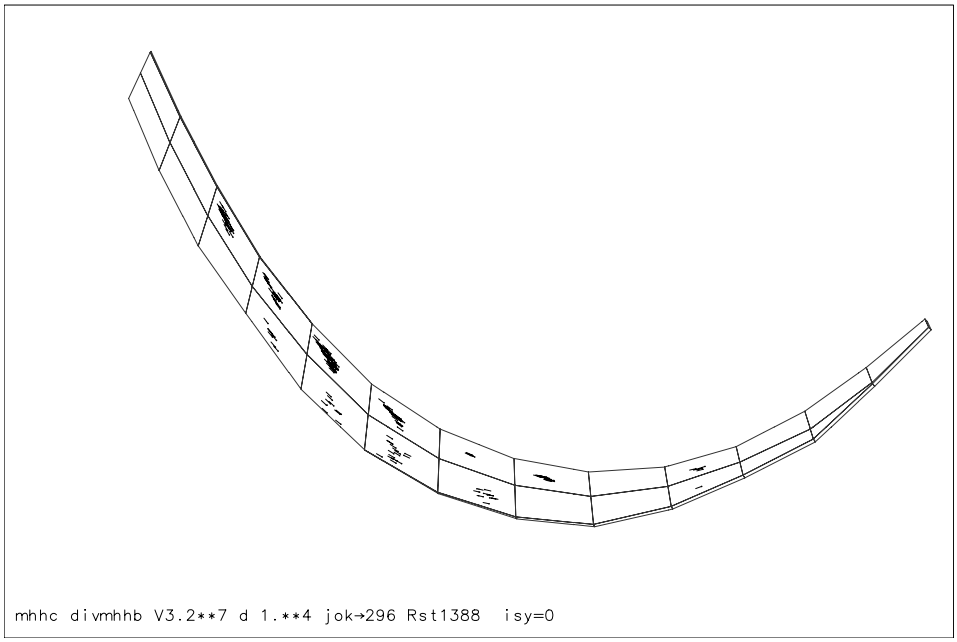

Figure 2.5-9. A 3-D view of the proposed divertor and baffle plates in relation to the LCFS (top) and impacts of field lines on the divertor target plates (bottom).

information on divertor configurations in helias-type devices is needed from W7-AS [50] and W7-X [49] in order to improve the divertor configuration needed for a reactor.

2.6. IMPROVEMENTS TO THE MHH PHYSICS BASIS

2.6.1. Validation of the MHH Physics Basis

Better physics understanding is needed for better extrapolation to a fusion power plant. The size and power (hence performance) of stellarators is not as advanced as in tokamaks, as indicated in Fig. 2.6-1. The most common measure of performance in tokamaks is $n\tau_E T_i(0)$. Using the definition of τ_E and the Lackner-Gottardi (gyro-reduced Bohm) scaling law [Eq. (2.4-3)]) gives

$$n\tau_E T_i(0) \quad \propto \quad V_p n^{1.2} B_0^{1.6} P^{-0.2} \iota^{0.8} \,, \tag{2.6-1}$$

where V_p is the plasma volume. If n is given by Eq. (2.4-6), then

$$n\tau_E T_i(0) \quad \propto \quad V_p^{0.4} B_0^{2.2} P^{0.4} \iota^{0.8} \,. \tag{2.6-2}$$

Higher values of $n\tau_E T_i(0)$ are obtained in present tokamaks because of their higher values for V_p, B_0, and P, rather than better confinement properties relative to the smaller stellarators.

However, this is expected to change as first LHD and then W7-X come into operation. LHD and W7-X will study a number of confinement scaling and transport issues needed for reactor extrapolation: (a) ambipolar electric fields and their role in transport at low collisionality, (b) bootstrap current minimization and compensation, (c) optimization of improved confinement modes, and (d) attainment of several keV ion temperatures and significantly higher values of $n\tau_E T_i$. Also, more information is needed from these experiments on the scaling of beta limits, their dependence on configuration properties, and MHD behavior at more reactor-relevant values of beta, $\langle\beta\rangle \approx 5\%$ versus the $\langle\beta\rangle \approx 2.1\%$ obtained at present. Experience on steady-state particle and power handling will be obtained from W7-X and LHD. In addition, information gained from the ergodic divertor experiments on Tore Supra will be useful because of the similarity to the edge island structure on MHH. Information on the pumping efficiency with an ergodic edge and magnetic islands is needed. It will also be necessary to lessen the power to the divertor plates through a radiative edge, as is being pursued on different tokamaks and on W7-AS.

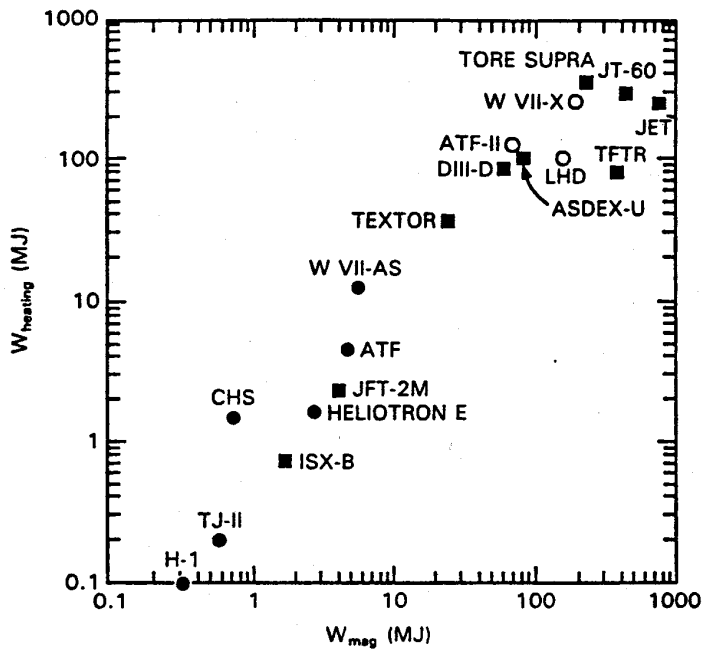

Figure 2.6-1. Comparison of the capabilities of representative tokamaks and stellarators in terms of the energy delivered to the plasma per pulse ($W_{heating}$) and the stored magnetic energy inside the plasma volume (W_{mag}). The solid circles represent present and near-term stellarators, the open circles represent the large next-generation stellarators, and the solid squares represent some comparable tokamaks.

2.6.2. Options for Configuration Improvement

The same plasma configuration can be obtained by any number of different coil configurations. This is achieved by moving and reshaping the toroidal coil winding surface using the NESCOIL code, which changes the properties of the region between the LCFS and the CWS. Small changes in the CWS can make the field-line topology in this outer region exhibit total chaos, large or small magnetic islands, or good flux surfaces. For example, Fig. 2.6-2 shows an MHH configuration which maintains the same plasma configuration as the reference MHH configuration, but displays large islands outside of the LCFS. These islands can be used for channeling flux to a divertor, or for shielding the leading edge of a pump-limiter head.

The freedom to vary the coil configuration is important since it can be used to implement different types of divertor designs or to change the engineering properties while maintaining the same physics properties. In addition, it should be possible to reduce

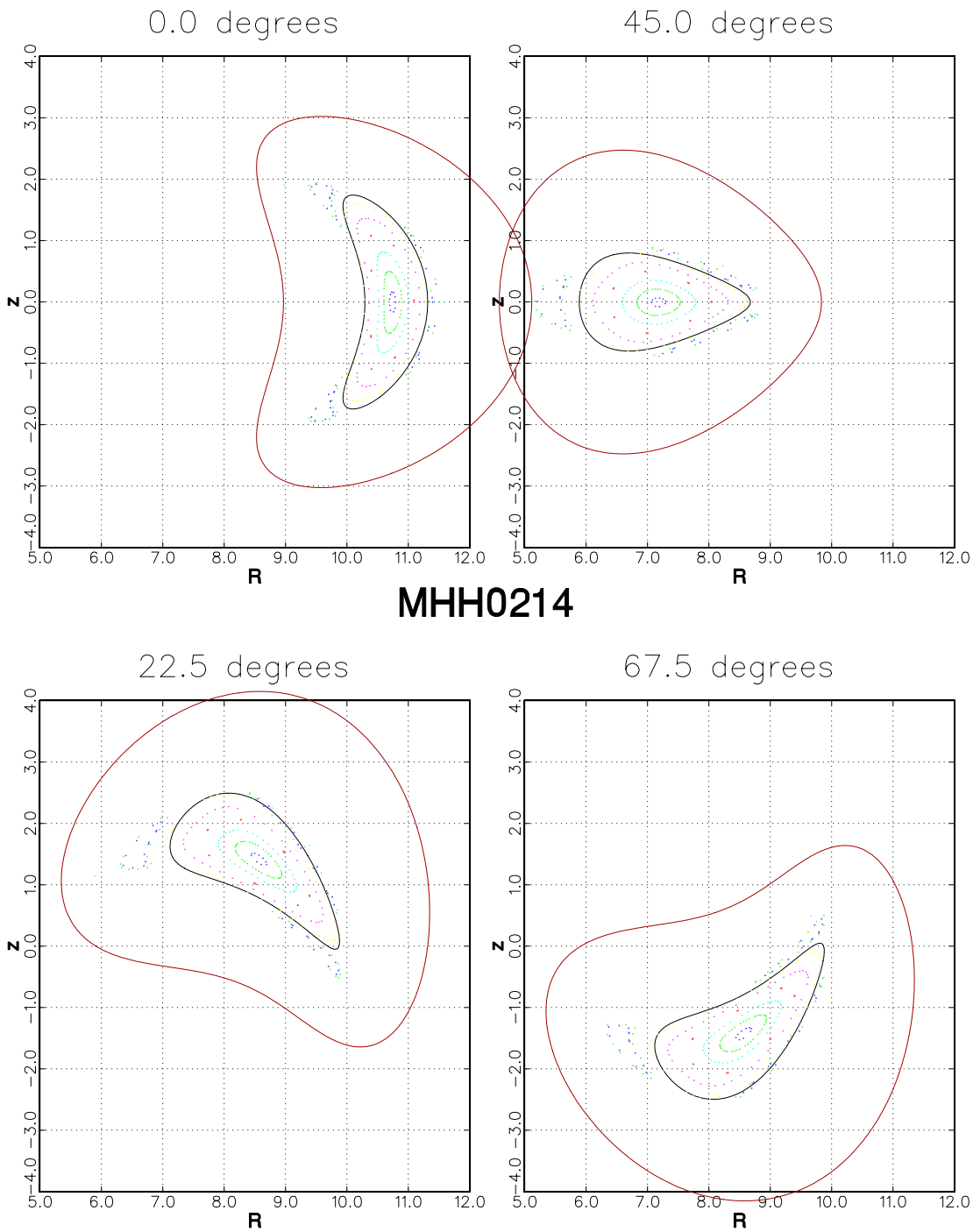

Figure 2.6-2. A variation of the basic MHH configuration that exhibits large islands outside of the LCFS. The LCFS is the same as in the base case – only slight changes to the CWS produced this difference.

the maximum field on the coils and to increase the bend radii. Additional space in the inside corner area and in the coil-plasma spacing could also lead to improved reactor candidates. Similarly, any reduction in the non-planar excursions of the coils themselves would be advantageous. More optimized designs were obtained in the course of the study after the configuration had been frozen for the engineering design summarized in this report; *e.g.,* an MHH configuration with negligible plasma currents, improved quasi-helical confinement properties, and $\langle\beta\rangle > 6\%$ [22]. A three-field-period, eight-coil-per-period version of MHH (described in the next section) has increased distance between coils on the congested inside corners, more plasma-coil spacing, better MHD properties, and lower plasma aspect ratio ($R_0/a_p = 6$). Thus it should be possible to make small modifications in the present MHH design to improve its engineering and physics properties.

2.6.3. The MHH3 Stellarator

Subsequent to selection of the particular MHH configuration used for the engineering design phase of the SPPS, Garabedian and Gardner [51] have continued investigations toward improvement over the reference MHH configuration. A new configuration, labelled MHH3, has been designed with three field periods that has a much reduced bootstrap current and allows for more space between the plasma and the coils.

As with the reference MHH, the plasma surface is specified by a set of Fourier coefficients $\delta_{m,n}$ where the r,z coordinates of the LCFS are given by

$$r + iz \;=\; \sum \delta_{m,n} e^{i(mu+3n\nu)} \,, \tag{2.6-3}$$

where u and ν are poloidal and toroidal angle-like variables. For MHH3, the expansion coefficients $\delta_{m,n}$ are given in Table 2.6-I.

Table 2.6-II contrasts the geometrical properties for the two MHH configurations. Figure 2.6-3 shows a top view of the filammentary MHH3 case, and Fig. 2.6-4 shows the resulting flux surfaces. This configuration offers the possibilities of smaller reactors, easier access to the divertor region, or reduced engineering complexities with respect to coil crowding. Most physical properties, including perturbative bootstrap current effects, turn out to be even better for this new case than those of the reference MHH design that was adopted; *e.g.,* it has near quasi-helical symmetry.

Calculations with the NSTAB nonlinear stability code [7] indicate that the equilibrium and stability limit on $\langle\beta\rangle$ for MHH3 is above 5%. However, there is no experimental data yet above $\langle\beta\rangle = 1.2\%$ for modular stellarators. Since this nonlinear stability test gives

Table 2.6-I.
Fourier Coefficients ($\delta_{m,n}$) for the MHH3 Plasma Surface

	$m=-3$	$m=-2$	$m=-1$	$m=0$	$m=1$	$m=2$
$n=-1$				0.20		0.13
$n=0$	0.02	0.02	0.05	6.00	1.	0.10
$n=1$		–0.05	–0.50	0.75	–0.15	
$n=2$	–0.02	0.09	–0.09	0.15	–0.035	
$n=3$		0.04		0.02		

the expected beta limits for the ITER and TPX tokamaks, it is a plausible tool to apply in the SPPS project.

Monte Carlo simulations of the MHH3 reactor using the TRAN computer code [8] show that the particle confinement time τ_p scales as $\rho_L^{-2.5}$, where ρ_L is the ion gyroradius measured in units of the plasma radius. For $B = 4$ T, $\langle T \rangle = 10$ keV, and $\langle n \rangle = 2 \times 10^{20}$ m^{-3}, the code estimates $\tau_p = 8$ s ($\tau_E = 2$ s if $\tau_p = 4\tau_E$ is assumed).

A primary direction for stellarator reactors is to minimize the effects of the bootstrap current. A new expression [51], developed by Garabedian and Gardner for the bootstrap current, relatively track those of the present theory, although the magnitudes of the results can differ appreciably. This new method permits rapid insight into how parameters of the design can be varied to accomplish this task. This has played a significant role in the optimization of the MHH3 configuration. Other variants of MHH have been found that possess a deep magnetic well (2%), low bootstrap current, and still have relatively large plasma-coil separations and smoother coils, needed for attractive reactors.

A possible reactor embodiment of the MHH3 has an average major radius of 13.5 m, a plasma radius of 2.25 m, and a gap of 2 m between the LCFS and the filamentary centerline of the modular coils. The coils themselves have reduced curvature as compared to the MHH case. There should be enough flexibility to allow for corrections that might become necessary after more detailed studies of alpha-particle containment and the divertor are made. However, given the limited resources and time constraints of this study, the SPPS was unable to develop this configuration.

Table 2.6-II.
Geometrical Characteristics of the MHH and MHH3 Configurations for the Same (2-m) Plasma to Coil-center Distance

	MHH	MHH3
Average major radius (m)	14	13.5
Plasma volume (LCFS) (m^3)	734	1,032
Plasma surface area (LCFS) (m^2)	1,233	1,442
Volume within coil winding surface (CWS) (m^3)	5,720	7,179
Area of CWS (m^2)	2,930	3,158

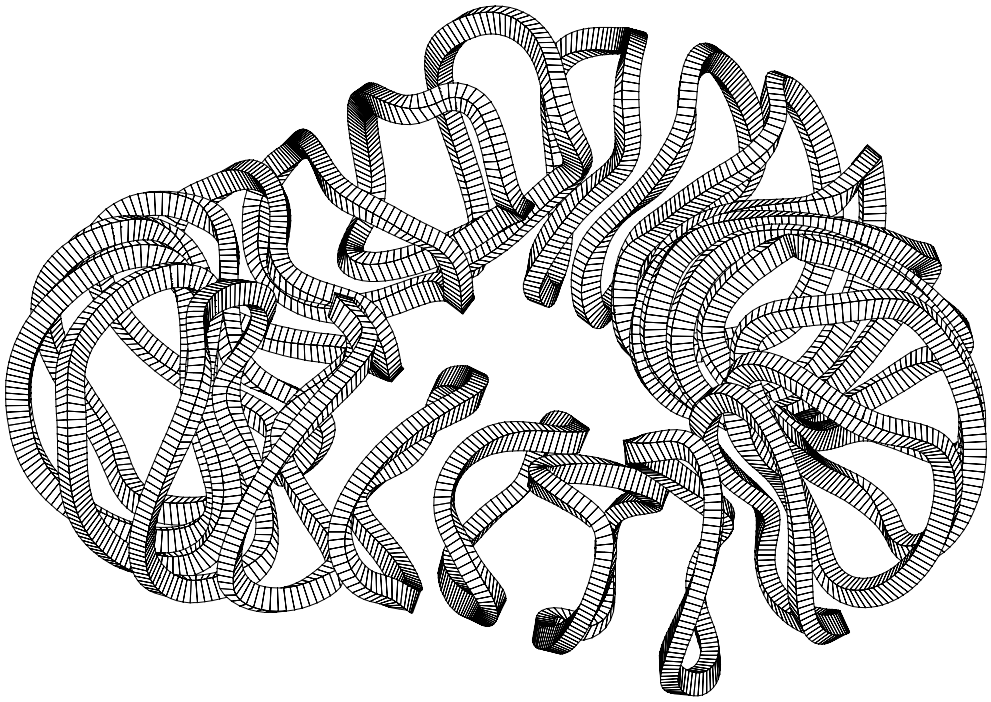

Figure 2.6-3. An oblique view of the coil set for MHH3, a three-field-period variant of the MHH configuration.

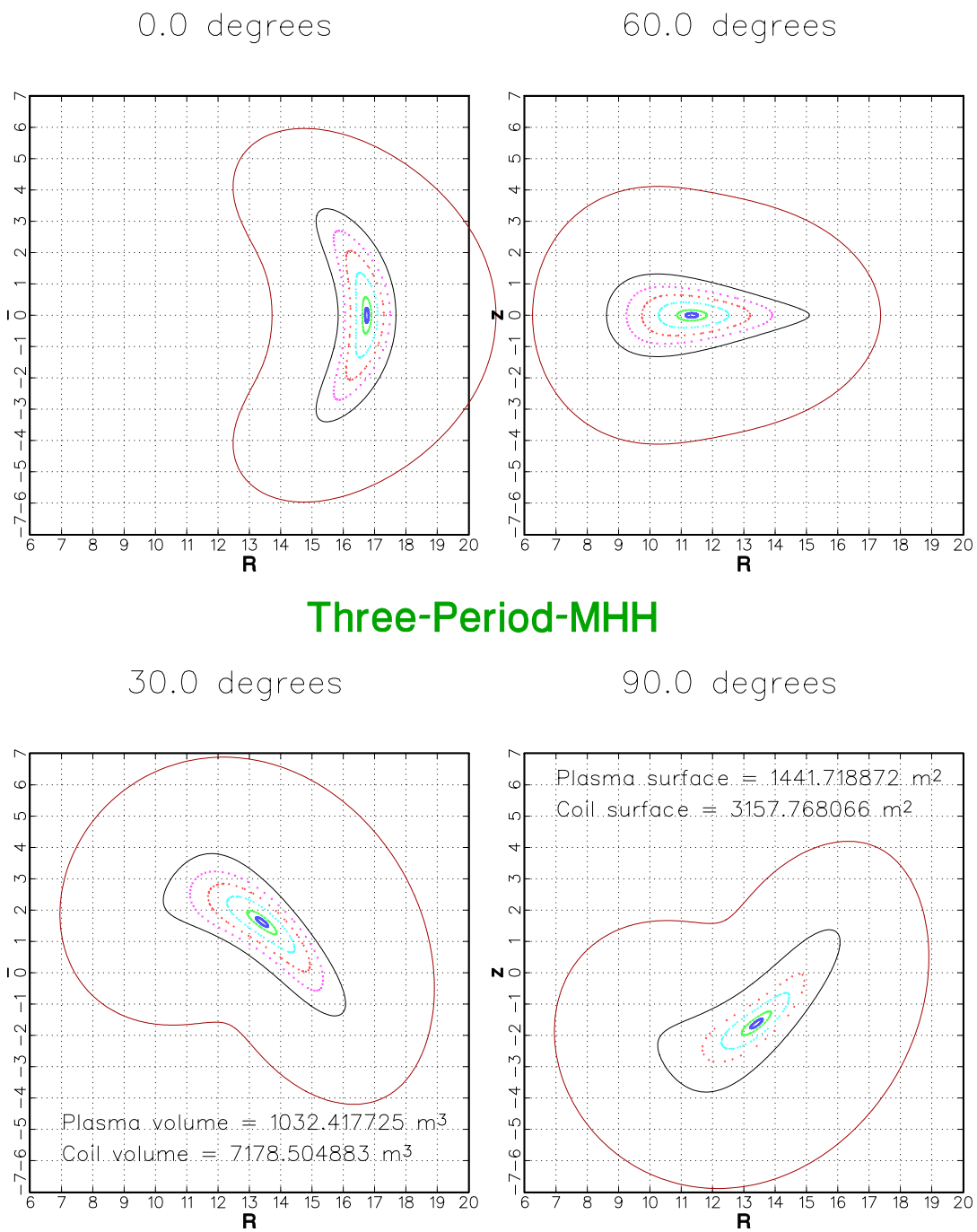

Figure 2.6-4. Flux surfaces for the three-field-period configuration of Fig. 2.6-3 at four toroidal angles in a 120° field period. This configuration increases the plasma-coil spacing for a given average major radius.

REFERENCES

[1] B. A. Carreras, G. Grieger, J. H. Harris, J. L. Johnson, J. F. Lyon, *et al.*, "Progress in Stellarator/Heliotron Research: 1981-1986," *Nucl. Fusion* **28** (1988) 1613.

[2] J. F. Lyon, "Near-Term Directions in the World Stellarator Program," *Fusion Technol.* **17** (1990) 19.

[3] J. Nührenberg and R. Zille, "Quasi-Helically Symmetric Toroidal Stellarators," *Phys. Lett. A* **129** (1988) 113.

[4] W. Lotz, P. Merkel, J. Nührenberg, A. Schlüter, and R. Zille, "Optimization of Helias for W VII-X," *Proc.* 7th *Int. Workshop on Stellarators,*, Oak Ridge, TN, April 1989, International Atomic Agency report IAEA-TECDOC-558, IAEA, Vienna (1990) p. 485.

[5] W. Lotz, J. Nührenberg, and C. Schwab, "Optimization, MHD Mode and Alpha Particle Confinement Behavior of Helias Equilibria," *Proc. 13th Int. Conf. on Plasma Phys. and Controlled Nucl. Fusion Research,* Washington, D.C. (Oct. 1990), International Atomic Energy Agency, Vienna (1991) p. 603.

[6] F. Bauer, O. Betancourt, and P. Garabedian, *Magnetohydrodynamic Equilibrium and Stability of Stellarators*, (Springer-Verlag, New York) (1984).

[7] M. Taylor, "A High-Performance Spectral Code for Nonlinear MHD Stability," *J. Comp. Phys.* **110** (1994) 407.

[8] P. Garabedian and M. Taylor, "Tokamak Transport Driven by Quasi-Neutrality and Helical Asymmetry," *Nucl. Fusion* **32** (1992) 265.

[9] P. Merkel, "Solution of Stellarator Boundary Value Problems with External Current," *Nucl. Fusion* **27** (1987) 867.

[10] A. H. Boozer, "Plasma Equilibrium with Rational Magnetic Surfaces," *Phys. Fluids*, **24** (1981) 1999; also R. H. Fowler, J. A. Rome, and J. F. Lyon, "Monte Carlo Studies of Transport in Stellarators," *Phys. Fluids* **28** (1985) 338.

[11] D. T. Anderson and P. R. Garabedian, "A Stellarator Configuration for Reactor Studies," *Nucl. Fusion* **34** (1994) 881.

[12] J. F. Lyon, K. Gulec, R. L. Miller, and L. El-Guebaly, "Status of the US Stellarator Reactor Study," *Fusion Eng. Des.* **25** (1994) 85.

[13] C. Beidler, G. Grieger, E. Harmeyer, *et al.*, "Reactor Studies on Advanced Stellarators," *Proc. 14th Int. Conf. on Plasma Phys. and Controlled Nucl. Fusion Research,* Würzburg, Germany (Oct. 1992), International Atomic Energy Agency, Vienna (1993) p. 327.

[14] A. P. Navarro, A. L. Fraguas, M. A. Ochando, and L. Garcia, "Size Optimization and Dynamics Studies for a Heliac Stellarator Reactor", *Proc.* 10*th Int. Conf. Stellarators,* Madrid, Spain, paper O28.

[15] B. A. Carreras, N. Dominguez, L. Garcia, *et al.*, "Low-Aspect-Ratio Torsatron Configurations," *Nucl. Fusion* **28** (1988) 1195.

[16] J. F. Lyon, J. A. Rome, P. R. Garabedian, and D. T. Anderson, "Physics Assessment of Stellarators as Fusion Power Plants," *Proc. 15th Int. Conf. on Plasma Phys. and Controlled Nucl. Fusion Research,* Seville, Spain (Sep. 1994), International Atomic Energy Agency, Vienna (1996).

[17] J. Nührenberg and R. Zille, "Stable Stellarators with Medium β and Aspect Ratio," *Phys. Lett. A* **114** (1986) 129.

[18] G. Grieger, E. Harmeyer, W. Lotz, *et al.*, "Modular Stellarator Reactors and Plans for Wendelstein 7-X," *Fusion Technol.* **21** (1992) 1767.

[19] G. Grieger, J. Nührenberg, H. Renner, J. Sapper, and H. Wobig, "HELIAS Stellarator Reactor Studies and Related European Technology Activities," *Fusion Eng. Des.* **25** (1994) 73.

[20] J. F. Lyon, B. A. Carreras, K. K. Chipley, *et al.*, "The Advanced Toroidal Facility," *Fusion Technol.* **10** (1986) 179.

[21] J. F. Lyon, B. A. Carreras, J. H. Harris, *et al.*, "Stellarator Physics Evaluation Studies," *Proc. 9th Int. Conf. on Plasma Phys. and Controlled Nucl. Fusion Research,* Baltimore, MD (1982), International Atomic Energy Agency, Vienna (1983) Vol. 3, p. 115.

[22] P. R. Garabedian, private communication (1994).

[23] F. Najmabadi, R. W. Conn, *et al.*, "The ARIES-II and -IV Second-Stability Tokamak Fusion Power Plant Study—The Final Report," UCLA report UCLA-PPG-1461 (to be published); also, F. Najmabadi, R. W. Conn, *et al.*, "Directions for Attractive Tokamak Reactors: The ARIES-II and ARIES-IV Second-Stability Designs," *Proc.*

14th Int. Conf. on Plasma Phys. and Controlled Nucl. Fusion Research, Würzburg, Germany (Oct. 1992), International Atomic Energy Agency, Vienna (1993) 295.

[24] E. Harmeyer, F. Herrnegger, J. Kisslinger, F. Rau, and H. Wobig, "Studies on MHH, the Modular Helias-like Heliac, and Some Comparisons to W7-X and HSR, the Helias Stellarator Reactor Derived from W7-X," IPP report (1994) (unpublished).

[25] S. P. Hirshman, W. I. van Rij, and P. Merkel, "Three-Dimensional Free Boundary Calculations Using a Spectral Green's Function Method," *Comput. Phys. Commun.* **43** (1986) 143.

[26] A. H. Reiman and H. S. Greenside, "Computation of Zero β Three-Dimensional Equilibria with Magnetic Islands," *J. Comput. Phys.* **87** (1990) 349.

[27] A. H. Glasser, J. M. Greene, and J. L. Johnson, "Resistive Instabilities in General Toroidal Plasma Configurations," *Phys. Fluids* **18** (1975) 875.

[28] M. Murakami, B. A. Carreras, L. R. Baylor, *et al.*, "Bootstrap Current Experiments in a Toroidal Plasma-Confinement Device," *Phys. Rev. Lett.* **66** (1991) 707.

[29] A. H. Boozer and H. J. Gardner, "The Bootstrap Current in Stellarators," *Phys. Fluids B* **2** (1990) 2408.

[30] D. E. Hastings, W. A. Houlberg, and K. C. Shaing, "The Ambipolar Electric Field in Stellarators," *Nucl. Fusion* **25** (1985) 445.

[31] S. Sudo, Y. Takeiri, H. Zushi, *et al.*, "Scalings of Energy Confinement and Density Limit in Stellarator/Heliotron Devices," *Nucl. Fusion* **30** (1990) 11.

[32] R. J. Goldston, H. Biglari, G. W. Hammett, *et al.*, "$\tilde{\mathbf{E}} \times \tilde{B}/B^2$ *vs.* $\mu_{\|}\tilde{\mathbf{B}}/B$ as the Cause of Transport in Tokamaks," *Bull. Am. Phys. Soc.*, **34** (1989) 1964.

[33] K. Lackner and N. A. O. Gottardi, "Tokamak Confinement in Relation to Plateau Scaling," *Nucl. Fusion* **30** (1990) 767.

[34] M. Murakami, private communication (1992).

[35] S. Kaye, private communication (1992).

[36] A. Iiyoshi, M. Fujiwara, O. Motojima, N. Ohyabu, and K. Yamazaki, "Design Study for the Large Helical Device, *Fusion Technol.* **17** (1990) 169.

[37] C. Beidler, *et al.*, "Physics and Engineering Design for Wendelstein VII-X," *Fusion Technol.* **17** (1990) 149.

[38] J. F. Lyon and S. L. Painter, "Assessment of Torsatrons as Reactors," Oak Ridge National Laboratory report ORNL/TM-12189 (1992).

[39] F. Wagner *et al.*, "Boundary Layer and H-Mode Studies in W7-AS," *Proc. 15th Int. Conf. on Plasma Phys. and Controlled Nucl. Fusion Research,* Seville, Spain (Sep. 1994), International Atomic Energy Agency, Vienna (1996).

[40] K. Toi, T. Morisaki, S. Sakakibara, *et al.*, "Impact of Rotational-Transform Profile Control on Plasma Confinement and Stability in CHS," *Proc. 15th Int. Conf. on Plasma Phys. and Controlled Nucl. Fusion Research,* Seville, Spain (Sep. 1994), International Atomic Energy Agency, Vienna (1996).

[41] J. F. Lyon, "Stellarator Optimization and Transport Studies," Stellarator Power Plant Workshop, Dallas (March 13, 1994).

[42] K. Gulec, "Physics and Cost Optimization of a Torsatron Reactor," M. S. thesis, University of Tennessee, Knoxville (May 1994).

[43] J. F. Lyon, S. L. Painter, L. M. Kovrizhnykh, and K. Gulec, "Stellarator Transport Optimization with Self-Consistent Electric Fields," *Proc. 21st EPS Conf. Controlled Fusion and Plasma Phys.,* Montpellier, France, June 1994, Vol 18B, Part I, p. 380.

[44] W. A. Houlberg, S. E. Attenberger, and L. M. Hively, "Contour Analysis of Fusion Reactor Plasma Performance," *Nucl. Fusion* **22** (1982) 935.

[45] A. M. Messiaen, J. Ongena, U. Samm, *et al.*, "Transport and Improved Confinement in High Power Edge Radiation Cooling Experiments in TEXTOR," *Proc. 15th Int. Conf. on Plasma Phys. and Controlled Nucl. Fusion Research,* Seville, Spain (Sep. 1994), International Atomic Energy Agency, Vienna (1996).

[46] EQUIPE TORE SUPRA, "Radiative Layer Experiments with an Ergodized Boundary in Tore Supra," *Proc. 15th Int. Conf. on Plasma Phys. and Controlled Nucl. Fusion Research,* Seville, Spain (Sep. 1994), International Atomic Energy Agency, Vienna (1996).

[47] T. Uckan, R. C. Isler, *et al.*, "Biased Limiter Experiments on the Advanced Toroidal Facility (ATF) Torsatron," *Nucl. Fusion* **34** (1994) 295.

[48] A. Komori *et al.*, "Local Island Divertor Concept for LHD," *Proc. 15th Int. Conf. on Plasma Phys. and Controlled Nucl. Fusion Research,* Seville, Spain (Sep. 1994), International Atomic Energy Agency, Vienna (1996).

[49] H. Renner, "Divertor Design for the Optimized Stellarator W7-X," Proceedings of the IEA Workshop on Technological Aspects of Steady-State Devices, Garching, Germany (Feb. 1995).

[50] Y. Feng *et al.*, "A Program for W7-X-Relevant Divertor Studies on W7-AS," Proceedings of the IEA Workshop on Technological Aspects of Steady-State Devices, Garching, Germany (Feb. 1995).

[51] P. Garabedian and H. Gardner, "Reduction of the Bootstrap Current in the Modular Helias-like Heliac Stellarator," *Physics of Plasmas* **2** (1995) 2020.